Electron Microscopy Study of the Phase Transformation and Metal Functionalization of Titanium Oxide Nanotubes

by

Sanjitarani Santra

A Dissertation Presented in Partial Fulfillment
of the Requirements for the Degree
Master of Science

Approved April 2014 by the
Graduate Supervisory Committee:

Peter A. Crozier, Chair
Ray Carpenter
Daniel Buttry

ARIZONA STATE UNIVERSITY

May 2014

ABSTRACT

Titanium oxide (TiO_2), an abundant material with high photocatalytic activity and chemical stability is an important candidate for photocatalytic applications. The photocatalytic activity of the TiO_2 varies with its phase. In the current project, phase and morphology changes in TiO_2 nanotubes were studied using *ex-situ* and *in-situ* transmission electron microscopy (TEM). X-ray diffraction and scanning electron microscopy studies were also performed to understand the phase and morphology of the nanotubes. As prepared TiO_2 nanotubes supported on Ti metal substrate were amorphous, during the heat treatment in the ex-situ furnace nanotubes transform to anatase at 450 ^oC and transformed to rutile when heated to 800 ^oC. TiO_2 nanotubes that were heat treated in an *in-situ* environmental TEM, transformed to anatase at 400 ^oC and remain anatase even up to 800 ^oC. In both ex-situ an in-situ case, the morphology of the nanotubes drastically changed from a continuous tubular structure to aggregates of individual nanoparticles. The difference between the *ex-situ* an *in-situ* treatments and their effect on the phase transformation is discussed. Metal doping is one of the effective ways to improve the photocatalytic performance. Several approaches were performed to get metal loading on to the TiO_2 nanotubes. Mono-dispersed platinum nanoparticles were deposited on the TiO_2 nanopowder and nanotubes using photoreduction method. Photo reduction for Ag and Pt bimetallic nanoparticles were also performed on the TiO_2 powders.

To

Late Yolanda Murphy

Page

LIST OF TABLES

LIST OF FIGURES

Chapter1

INTRODUCTION

1.1 General background

1.1.1 Light harvesting to meet the energy crisis

According to United States Census Bureau[1], the world population is growing at a rate of 1.2%, or approximately 80 million people per year. With one birth every 8 seconds and one death every 12 seconds, the world is becoming more populated each second. The energy consumption will rise faster by 56% from 524 quadrillion BTU in 2010 to 820 quadrillion BTU in 2040[2]. Fossil fuels such as petroleum, natural gas, and coal will makeup more than 80% of energy sources, but these energy sources remain in limited geographies. Fossil fuels generate large quantities of carbon dioxide gas (CO_2) and other gases, which can upset the atmospheric composition. Nuclear energy does not generate CO_2 and can be implemented in many regions of the world, but is losing popularity, especially in the United States, where no new nuclear power plants have been ordered since the Three Mile Island accident in 1979 and no long-term waste storage strategy has been implemented.

Renewable energy is an alternative that is considered to be safe for both the short and long terms and scales from portable applications such as small electronics to large applications such as automobiles and power plants. Renewable energy such as wind and solar energy do not generate CO_2. Plants utilize solar energy and use green pigments as catalysts. In order to harvest solar energy for human usage successfully, effective catalysts are necessary for solar energy based reactions[3]. Photocatalysis is the field in active research of improving and understanding photoreactions and associated catalysts.

1.1.2 Photocatalysis (heterogeneous) fundamental

A photocatalysis process is essentially a photoreaction in the presence of a catalyst. Photosynthesis is the classic natural photocatalysis process, where chlorophylls are the catalysts. A semiconductor based heterogeneous photocatalysis process is composed of three steps: excitation, electron-hole pair creation and oxidation-reduction.

The first step is excitation; upon suitable light application. In a semiconductor a bandgap is available, which is essentially the gap between top of valence band and bottom of conduction band. Upon light of enough energy is provided to a semiconductor, excitation occurs.

The second step is electron and/or energy transfer in a deexcitation process. Electrons from the occupied level of donor reactant transfers to an unoccupied acceptor reactant level. Upon photon excitation, an electron-hole pair is generated which recombine unless otherwise other reaction sites are available. The lifetime of such recombination is in the order of nanoseconds[4]. After electron-hole pair creation, recombination can occur either inside the volume of the semiconductor or on the surface. Alternatively, the electron can travel to find an acceptor on the surface, and a donor may find a hole on the surface.

The final step is the chemical reaction of oxidation and reduction occurring on surface. In this step an electron and hole, which reach the catalyst surface, interact with redox species to form intermediate or final products. For instance, in a Pt functionalizes TiO_2 based water splitting reaction, electrons and holes are involved at reduction and oxidation steps as represented in the chemical equations[5].

$OH^- + h^+ \rightarrow O_2$

$H^+ + e^- \rightarrow H_2$

The success of acceptor and donor excitation, or in other words, the electron – hole transfer to the suitable reaction sites, depends on the availability of reaction sites and the band gap position with respect to the molecular energy level of the reaction molecule. The band edge position of the semiconductor is very important for successful electron transfer from conduction band to the redox potential level of the reactant molecule. Fig. 1.1 presents the relative position of different semiconducting band edges with respect to the hydrogen electrode[4]. These values were obtained in contact with aqueous solution at a pH value of 1. For a reduction reaction to be successful, band edge position of the reaction species should be situated lower to the band edge of semiconductor. In other words, the semiconductor band edge should have more negative reduction potential value.

Apart from the above factors, other factors also influence the success of electronic transfer between semiconductor and reactant species, or in other words, the catalytic efficiency of the system. These factors include presence of electron traps, surface area and size of the catalyst. Surface defects act as shallow electron traps and hence acts as holes for capturing electrons before they are available to surface catalysis reactions. By annealing the semiconductor catalysts the surface defects are often removed and electron-hole recombination time is improved[6].

1.1.3 TiO_2

Fujishima and Honda[7] discovered the photocatalytic properties of TiO_2 electrodes for the water splitting reaction in 1972. Ever since, research has been conducted in

understanding the fundamental properties of photocatalysis and TiO_2. TiO_2 is abundant in nature, chemically stable, non hazardous in properties, and inexpensive. Hence it has become a suitable choice in chemistry, materials science and engineering in catalysis research. In the past decades, TiO_2 has seen application in energy storage[8], energy renewal[9], and environmental cleaning[10-12].

Anatase and rutile are the two common phases of TiO_2, with a more rare phase of brookite, which is the least, studied among three. Between anatase and rutile, the latter is thermodynamically more stable at higher temperature. Both anatase and rutile share a tetragonal crystal structure, while the later is a denser one. A few basic physical properties of anatase and rutile are summarized in Table 1.1[12].

1.1.4 TiO_2 nanotubes

TiO_2 nanotubes were initially prepared via a template synthesis route[13] around in 1996 followed by in hydrothermal method[14] in 1998. Anodic synthesis was developed later around in 2001 by Grimes group.[15] In a general TiO_2 mediated mechanism, electron transport is a significant limiting factor in photocatalysis and is governed and influenced by the structural architecture of TiO_2. TiO_2 nanotubes in particular yield enhanced catalytic activity as they provide a larger surface area and shorter electron-hole migration paths to the surface compared to other forms of TiO_2[16]. Hollow TiO_2 nanotubes demonstrate a superior electron transport and help in improving the catalytic efficiency[16]. TiO_2 nanotubes have also wide applications in other areas such as dye sensitized solar cells[3,17] and gas sensing devices[18-19].

1.1.5 Improving catalytic efficiency of tubes

There are methods to improve the catalytic efficiency of TiO_2 tubes. Metal/nonmetal doping is an effective method to improve the photocatalytic performance. Doping may change the band gap[20] and in some cases make the material active in the visible region[21]. According to work by Umebayashi et al.[20], sulfur doping of TiO_2 resulted in shifting the band edge to lower energy. Metal functionalization helps in trapping electrons, which helps reduce electron-hole pair recombination; this enhances the photocatalytic activity. There are different ways to functionalize a catalyst. Impregnation is one of the traditional choices[22] among wet synthesis methods, in which the catalyst is impregnated with desired metal precursor solution followed by drying, calcination, and reduction in suitable gas and temperature environments. In gas method, chemical vapor deposition is a choice. The limitations of this method are discussed in chapter 4.2.2. Photoreduction is another method to functionalize ceramic catalysts. TiO_2 is known to reduce metal ions to their respective elemental metals[23-24] using free electrons on its surface, in the presence of suitable conditions – light illumination and/or chemical environments. Photoreduction method has advantages over other methods owing to its simplicity; for example it does not require post reduction treatments as in impregnation technique.

1.2 Scope of thesis

Studies have reported on the catalytic performance of the polymorphs of TiO_2. For example, Kawahara et al.[25] reported the oxidation of CH_3CHO on anatase-rutile bilayer films and found the presence of both phases perform better than the individual films. Zhang et al.[26] found similar results in the reaction of H_2 evolution from

water/methanol solution that the anatase-rutile mixture performs better than the individual phases. Hurum et al.[27] have studied and found similar results on the anatase-rutile mixture. However, Tanaka et al. [28] reported that anatase is a better catalyst than rutile in the reaction of phenol degradation. Since both the morphology as well as the phase are critical to the catalytic activity of these nanotubes, it is important to determine the conditions where desired phase and morphology can be achieved.

In order to functionalize TiO_2 nanotubes, impregnating and soaking techniques have been successfully employed to generate dispersions of Pd particles inside nanotubes with a particle size of about 10 nm[29]. Such techniques also involve calcination and reduction heat treatments to convert metal precursor to metal nanoparticles. These treatments may change the morphology of the TiO_2 tubes because they are not structurally stable at higher temperatures, especially in a reducing environment[30]. Sputtering can be effectively used to deposit metal onto the mouths of the tubes but the resulting dispersion is not uniform[31]. Photoreduction is a potential approach for functionalizing tubes since it avoids high temperature heat treatments. Ni, Cu and Pt nanoparticles have been deposited onto TiO_2 powders using a photoreduction process[32-34].

This thesis discusses two major topics - TiO_2 nanotubes morphology and phase study as well functionalizing with different metals. The third chapter discusses in detail how heat treatments transform tubes into different phases and structures. Different characterization techniques are employed to understand the relationships of structure with treatment environments. The structures are also compared in both *ex-situ* and *in-situ* transmission electron microscopy (TEM) studies. The fourth chapter focuses on a one step Pt metal functionalization of tubes and characterization via scanning transmission

electron microscopy (STEM). In chapter five, Ag functionalization as well as some bimetallic results are discussed. In an appendix, supplementary results are discussed including the photocatalystic performances of tubes and metal functionalized tubes using a dye degradation reaction.

Table 1.1 Important physical properties of anatase and rutile phases

Property	Anatase	Rutile
Crystal structure	Tetragonal	Tetragonal
Space group	$I^4/_amd$	$P^4{}_{2/m}$ nm
Atoms per unit cell (z)	4	2
Lattice parameter (nm)	a = 0.3785, c = 0.9514	a = 0.4594, c = 0.2958
Unit cell volume (nm^3)	0.1364	0.0624
Density (kg m^{-3})	3894	4250
Band gap, experimental, (eV) (nm)	 ~3.2 ~387	 ~3.0 ~413

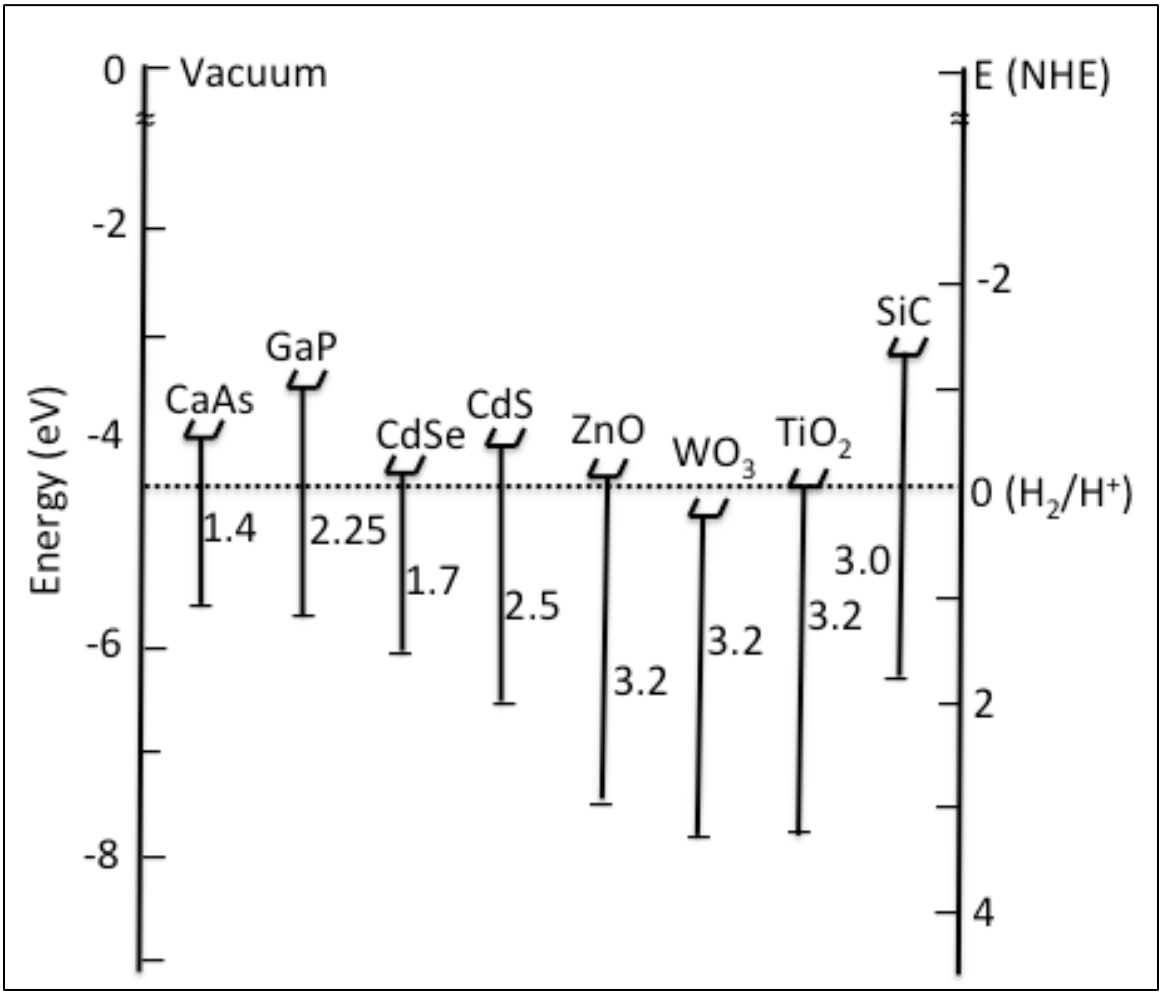

FIG. 1.1. Relative band edge positions of semiconductors in aqueous electrolyte at pH =1.[4]

Reference

1. World population growth rates 1950 - 2050. *United States Census Bureau* (2011).

2. World energy demand and economic outlook. *International Energy Outlook* (2013)

3. M. Adachi, Y. Murata, I. Okada, and S. Yoshikawa: Formation of Titania Nanotubes and Applications for Dye-Sensitized Solar Cells. *J. Electrochem. Soc.* **150**, G488 (2003)

4. A.L. Linsebigler, G. Lu, J. T. Yates: Photocatalysis on TiO_2 surfaces: Principles, Mechanims and Selected results. *Chem. Rev*. **95**, 735 (1995)

5. M. Matsuka, M. Kitano, M. Takeuchi, K. Tsujimaru, M. Anpo and J.M. Thomas: Photocatalysis for new energy production:Recent photocatalytic water splitting reactions for hydrogen production. *Cata. Today* **122**, 51 (2007)

6. S. Nakade, M. Matsuda, S. Kambe, Y. Saito, T. Kitamura, T. Sakata, Y. Wada, H. Mori, S. Yanagida: Dependence of TiO2 nanoparticle preparation methods and annealing temperature on the efficiency of dye-sensitized solar cells. *J. Phys. Chem. B.* **106**, 10004 (2002)

7. A. Fujishima, K. Honda: Electrochemical photolysis of water at semiconductor electrode. *Nature.* **238**, 37 (1972)

8. G.D. Moon, J. B. Joo, M. Dahi, H. Jung, Y. Yin: Nitridation and layered assembly of hollow TiO_2 shells for electrochemical energy storage. *Adv. Funct. Mater.* **24**, 848 (2014)

9. S.K. Deb: Dye-sensitized TiO2 thin-film solar cell research at the National Renewable Energy Laboratory (NREL). *Sol. Energ. Mat. Sol. C.* **88**, 1 (2005)

10. Y. Ohko, Y. Utsumi, C Niwa, T. Tatsuma, K. Kobayakawa, Y. Satoh, Y. Kubota, A. Fujishima: Self-sterilizing and self-cleaning of silicone catheters coated with TiO_2 photocatalyst thin films: a preclinical work. *J. Biomed. Mater. Res.* **58**, 97 (2001)

11. A. Fujishima, K. Hashimoto, T. Watanabe: TiO_2 photocatalysis fundamentals and applications. *BKC Inc.* (1999)

12. D. A. H. Hanaor, C.C. Sorrell: Review of anatase to rutile phase transformation. *J Mat Sc*. 46, 855 (2011)

13. P. Hoyer: Formation of a Titanium Dioxide Nanotube Array. *Langmuir* **12**, 1411 (1996)

14. T. Kasuga, M. Hiramatsu, A. Hoson, T. Sekino, and K. Niihara: Formation of Titanium Oxide Nanotube, *Langmuir* **14**, 3160 (1998)

15. D. Gong, C. A. Grimes, and O. K. Varghese: Titanium oxide nanotube arrays prepared by anodic oxidation. *J. Mater. Res.* **16**, 3331 (2001)

16. M. Adachi, Y. Murata, M. Harada, and S. Yoshikawa: Formation of Titania Nanotubes with High Photo-Catalytic Activity. *Chem. Lett.* **29**, 942 (2000).

17. K. Zhu, N. R. Neale, A. Miedaner, and A. J. Frank: Enhanced Charge-Collection Efficiencies and Light Scattering in Dye-Sensitized Solar Cells Using Oriented TiO2 Nanotubes Arrays. *Nano Lett.* **7**, 69 (2007)

18. O. K. Varghese, D. Gong, M. Paulose, K. G. Ong, and C. A. Grimes: Hydrogen sensing using titania nanotubes. *Sens. Actuators, B.* **93**, 338 (2003)

19. M.-H Seo, M. Yuasa, T. Kida, Y. Kanmura, J.-S. Huh, N. Yamazoe, and K. Shimanoe: Gas sensor using noble metal-loaded TiO_2 nanotubes for detection of large-sized volatile organic compounds. *J. Ceram. Soc. Jpn.* **119**, 884 (2011)

20. T. Umebaysh, T. Yamaki, H. Itoh, K. Asai: Band gap narrowing of titanium dioxide by sulfur doping. *Appl. Phys. Lett.* **81,** 454 (2002)

21. M. Kitano, M. Matsukoa, M. Ueshima, M. Apno: Recent developments in titanium oxide-based photocatalysts. *Appl. Catal. A-Gen*. **325**, 1 (2007)

22. G. Ertl, H. Knozinger, and J. Weitkamp: Handbook of heterogeneous catalysis, Vol 1. Wiley-VCH (1997)

23. T. Alammar, A-V. Mudring: Facile preparation of Ag/ZnO nanoparticles via photoreduction. *J. Mat. Sc.* 44, 3218 (2009)

24. S. Yu, X. Peng, G. Cao, M. Zhou, L. Qiao, J. Yao, H. He: Ni nanoparticles decorated titania nanotube arrays as efficient nanoenzymatic glucose sensor. *Electrochim. Acta*. **76**, 512 (2012)

25. T. Kawahara, Y. Konishi, H. Tada, N. Tohge, J. Nishii, and S. Ito: A patterned TiO_2(Anatase)/TiO_2(Rutile) bilayer-type photocatalyst: Effect of the Anatase/Rutile junction on the photocatalytic activity. *Angew. Chem., Int. Ed*. **41**, 2811 (2002)

26. J. Zhang, Q. Xu, Z. Feng, M. Li, and C. Li: Importance of the relationship between surface phases and photocatalytic activity of TiO_2. *Angew. Chem., Int. Ed*. **47**, 1766 (2008)

27. D.C. Hurum, A.G. Agrios, K.A. Gray, T. Rajh and M.C. Thurnauer*:* Explaining the enhanced photocatalytic activity of Degussa P25 mixed-phase TiO_2 using EPR. *J. Phys. Chem. B*. **107**, 4545 (2003)

28. K. Tanaka, M. F.V. Capule and T. Hisanaga: Effect of crystallinity of TiO_2 on its photocatalytic action. *Chem. Phys. Lett***. 187,** 73 (1991)

29. S. K. Mohapatra, N. Kondamudi, S. Banerjee, M. Misra: Design of a Highly Efficient Photoelectrolytic Cell for Hydrogen Generation by Water Splitting: Application of TiO_2-xCx Nanotubes as a Photoanode and Pt/TiO_2 Nanotubes as a Cathode. *J. Phys. Chem. C*, **111**, 8677 (2007)

30. S.Santra, S. Chenna, P. A. Crozier. (manuscript to be submitted).

31. A. Roguska, A. Kudelski, M. Pisarek, M. Lewandowsk, M. Dolata, M. Janik-Czachor: Raman investigations of TiO_2 nanotube substrates covered with thin Ag or Cu deposits. *J. Raman Spectrosc.* **40**, 1652 (2009)

32. J. L. Rodrígueza, M. A. Valenzuelaa, F. Polac, H. Tiznadod, T. Poznyak: Photodeposition of Ni nanoparticles on TiO_2 and their application in the catalytic ozonation of 2,4-dichlorophenoxyacetic acid. *J. Mol. Catal. A: Chem.* **353-354**, 29 (2012)

33. J. W. M. Jacobs, F. W. H. Kampers, J. M. G. Rikken, C. W. T. Bulle-Lieuwma, D. C. Koningsberger: Copper Photodeposition on TiO2 Studied with HREM and EXAFS. *J. Electrochem. Soc.* **136**, 2914 (1989)

34. F. B. Li, X. Z. Li: The enhancement of photodegradation efficiency using Pt–TiO_2 catalyst. *Chemosphere* **48**, 1103 (2002)

CHAPTER 2

INSTRUMENTATION

2.1 Introduction

In this chapter, the techniques used to characterize and study TiO_2 nanotubes and metal functionalized anatase nanoparticles are described. For surface morphology and tube parameters, scanning electron microscopy (SEM) was used. Phases in bulk were detected using X-Ray diffraction (XRD) whereas nanosized phases were studied by transmission electron microscopy (TEM). Electron energy loss spectroscopy (EELS) was used as a confirmatory tool to distinguish between different phases of TiO_2. Energy dispersive spectroscopy (EDS) was used to detect and quantify metals at the nanolevel in the TEM. For *in-situ* experiments of TiO_2 tubes, environmental TEM was used. Chemically sensitive imaging was performed with scanning transmission electron microscopy (STEM).

2.2 X-Ray diffraction

X-ray diffraction is a very useful tool for identification and study of crystallinity in solids[1,2]. X-rays are generated when high energy charged particle, e.g. electrons collide with matter. High energy electrons are capable of knocking out the inner shell electron that creates a hole. An outer shell electron fills the hole and by doing so the energy difference between the two states is dissipated as radiation known as X-ray. Depending on the states involved, the nomenclature for X-ray is decided. For example, 2p→ 1s transition gives a K_α line whereas a 3p→ 1s transition results in K_β X-ray. The energy associated with each X-ray is a characteristic value for a particular element. In XRD, we use a single characteristic wavelength to form the X-ray beam, such as Cu K_α. The X-ray

beam is directed onto the sample and we measure the angles the beam is scattered through as it passes through a sample.

Single and polycrystalline materials have a regularly repeating pattern of atoms. When a radiation has similar wavelength as the interatomic separation in a crystal, the crystal can act just as an optical grating and diffract radiation. The diffraction of X-rays by a crystal can be understood by Bragg's equation. Braggs's equation is expressed as

$$n\lambda = 2d\text{Sin}\Theta$$

where, n= integer number

λ= wavelength of X-ray

d= interplanar distance

Θ= angle of diffraction

For a certain type of crystal system the pattern of diffraction is unique. Two important phenomena govern such unique pattern. (A) Systematically absent reflection (B) Intensity of peaks. (A) The peaks obtained from X-ray diffraction are from several set of planes. Sometime a certain set of plane in a certain crystal system gives zero intensity i.e. the peak is absent. For example for a body centered cubic crystal, the signal for (100) plane is absent because at the Bragg's angle for (100) planes, the body center atom which lie midway between adjacent (100) planes diffract X-ray exactly 180° out of phase relative to the corner atoms on the (100) plane. The interference of diffracted waves is destructive and no signal is detected. On the other hand, strong peak is found for (200) planes for bcc type due to constructive interference of waves out of adjacent planes. (B) Intensity of a peak depends on the density of the atoms present in the corresponding plane. The

intensity of the reflection is higher when more atoms are present, which diffract the X-ray.

Figure 2.1 shows important components of a powder diffractometer. It consists of a source for X-ray (generally Cu Kα radiation of wavelength = 0.154 nm is used). The incident beam of X-ray passes through a filter to fall on the sample placed on a goniometer (sample stage). The diffracted beam is recorded as the sample is rotated. During a continuous scan, both source and detector are driven at constant angular velocity though increasing value of Θ and hence the source and the detector move at angle 2Θ relative to one another. For a step scan the angular step size and time duration of each movement source and detector can be set. In each case, the detector finally plots a graph between intensity and angle of diffraction.

2.3 Transmission electron microscope

Transmission electron microscopy (TEM) is an important tool for characterizing nanomaterials[3,4,5]. In TEM, an electron beam of 100 - 400 keV energy is incident on a thin, electron transparent sample placed in the vacuum chamber of the instrument. The electron beam impinges the sample using parallel illumination to form a magnified image with electromagnetic lenses. Electrons are emitted from the tip of a Schottky field emitter and accelerated to the incident beam energy. The condenser lenses in conjunction with a condenser aperture control the beam spread on the sample and also control the convergence angle and beam current onto the specimen. The specimen sits inside a twin objective lens. The first lens after the specimen is the imaging lens and is often called the objective lens. The next lens is the diffraction or intermediate lens, which switches its focal point to the imaging plane of the objective lens or the back focal plane of the

objective lens, where the diffraction pattern lies. The last 3-4 lenses are known as intermediate and projector lenses. These lenses magnify the image or diffraction pattern to a convenient magnification for the screen or other detectors such as the CCD[3]. Several apertures lie below the specimen. The objective aperture is used to select diffraction beams that contribute to the image. The selected area aperture is used to select an imaging region that contributes to a diffraction pattern.

Several signals generated from the electron sample interaction can be used to form an image, diffraction pattern and spectroscopy analysis. The transmitted and Bragg scattered electrons are collected for conventional imaging techniques such as bright field (BF TEM), dark field (DF TEM), and electron diffraction[3]. If both the transmitted and Bragg scattered beams are collected in imaging mode with a parallel beam, this is referred to as phase contrast imaging or high resolution transmission electron microscopy (HRTEM)[3]. Images obtained in both BF TEM and HRTEM images are discussed in this thesis. Inelastic scattered electrons and x-rays can be used for electron energy loss spectroscopy (EELS) and energy dispersive x-ray spectroscopy (EDS).

The final imaging technique we utilized is annular dark field scanning transmission electron microscopy (ADF STEM). In ADF STEM, a focused convergent beam with a semi-angle of ~10 mrad is scanned on a TEM transparent sample[3,5]. The transmitted and Bragg scattered beams are passed through the hole of the annular dark field detector while the high angle (> 50 mrad) incoherently scattered electrons are collected on the ring detector. This is often referred to as high angle annular dark field (HAADF) STEM[3,5]. Since all of the characteristic Bragg scattered beams are not collected, there is little diffraction contrast in the image. Instead, the contrast is

chemically sensitive and depends on the average atomic number of the specimen. Heavy atomic columns scatter stronger, and appear bright white on a HAADF STEM image, whereas light atomic columns such as carbon or oxygen are nearly invisible or black in images. HAADF STEM was used to obtain images of metal supported TiO_2 catalyst, which will be discussed later in this thesis. Figure 2.2 shows a schematic diagram and photograph of a JEOL 2010F TEM/STEM used in this thesis.

2.3.1 Energy dispersive x-ray spectroscopy

X-rays generated from the electron-specimen interaction are collected in energy dispersive x-ray spectroscopy (EDS) which contain chemical information of the sample[3,6]. An incident electron can ionizes the atom by removing one of the bound electrons leaving the atom in an excited state. For example, consider a K-shell electron which is removed by the incident electron; this will leave a vacancy in the K-shell. The ion can lower its energy by filling the vacancy with an electron from the outer shell and the excess energy is radiated as a characteristic X-ray. This characteristic X-ray energy is unique to the specific atom, which can be used to identify the elements present in the sample. The main component of the EDX is the x-ray detection unit, which is made of semiconductor material. X-rays from the sample hit the detector generating electron-hole pairs; the number of electron-hole pairs generated is proportional to the energy of the x-rays. The number of electron-hole pairs is detected by the detector and converted into a signal. The detector is cooled to liquid nitrogen temperature to deactivate the electron-hole pair generation due to thermal energy; this will help in keeping the noise levels very low while detecting the x-ray signal.

EDX can detect all the elements with an atomic number greater than 4. EDX can be used for both qualitative and quantitative analysis. The position of the peak on the energy scale can be used to identify the elements present in the sample. Quantitative analysis in EDX can be performed using Cliff-Lorimer equation. For example, the elemental ratio in a bimetallic nanoparticle can be used by using the following Cliff-Lorimer equation,

$$C_A/C_B = k * I_A/I_B$$

where C_A and C_B are the concentrations of elements A and B respectively in the sample and I_A and I_B are the intensities of the characteristic peaks from elements A and B respectively. 'k' is a sensitivity factor that depends on the atomic number correction factor, x-ray absorption within the sample, and x-ray fluorescence within the sample.

2.3.2 Electron energy loss spectroscopy

Electron energy loss spectroscopy (EELS) measures the energy lost to beam electrons though inelastic scattering events as they transmit through a specimen[3,7]. A small fraction of the inelastic losses are characteristic, especially when the beam electron transfers energy to the core level electrons. These core level electrons are promoted to higher unoccupied states. These measured losses are called core loss electrons and often contain characteristic features in the edges called energy loss near edge structure. EELS measures the density of unoccupied states Making EELS sensitive to the bonding states and structure of the material sampled. Most spectra in the TEM are measured over the range from 0 eV to ~2000 eV energy loss. The scattering cross section for losses greater than ~2000 eV is very low and the ability for current detectors to distinguish these losses from noise in the detector is low, despite the high collection efficiency due to the forward

scattering nature. Most EELS research focuses on elements within the first row of transition metals or lighter on the periodic table of elements, while EDS or other tools such as RBS and XPS may detect heavier elements. The energy resolution of EELS is depends on the electron source, stability of high tension and the microscope, and the number of pixels available on the CCD detector. For most cases, the energy resolution is approximately 1 eV. In contrast to EDS, the energy resolution is two orders of magnitude greater. The energy resolution of EELS can be improved by using a microscope with a cold field emission gun and/or an electron monochromator.

2.4 *In-situ* environmental transmission electron spectroscopy

In-situ environmental TEM (ETEM) is a powerful tool to study the gas-solid interactions at the nanoscale[8]. It helps in studying the real time changes taking place in the catalyst or supported metal catalysts under reactive gas conditions. This kind of information provides fundamental insights into phase transformation and metal support interactions. *In-situ* ETEM experiments were performed in an FEI Tecnai F20 field emission TEM operating at 200kV with a point resolution of 0.24 nm and an information limit of 0.14 nm. This instrument is capable of performing both TEM and STEM under reacting gas conditions. It is equipped with Gatan imaging filter, this allows us to follow *in-situ* nanoscale chemical changes using electron energy loss spectroscopy.

Figure 2.3, shows the external gas handling system connected to the TEM. The gas handling system consists of a mixing tank, from which gas flows along a stainless tube and a leak valve is used to control the amount of gas flowing into the microscope column. A mixing tank allows gases of arbitrary composition to be mixed from up to 4 different gases. Air used in our experiments is of 99.999% purity.

This microscope is equipped with a differential pumping system for holding gas pressures near the sample region of the microscope and at the same time protects the electron gun from damage because of exposure to high gas pressures. Figure 2.13 shows the schematic of the differential pumping system, this system is capable of handling gas pressures of up to 8 Torr. Gas is introduced in the sample area through the leak valve and the escape rate into the rest of the TEM column is restricted by small differential pumping apertures of 100 μm in size. Gas leaked through these apertures is pumped using a turbo molecular pump (1^{st} level of pumping) and a molecular drag pump (2^{nd} level of pumping). The small opening of the differential pumping apertures helps in holding high gas pressures near the sample region of the microscope.

Heating the samples was performed using a Gatan heating holder with a furnace body made of inconel. This holder is capable of going up to 900^{o}C in vacuum and the maximum temperature it can go in presence of gases depends on the type of gas and its pressure. The heating holder is equipped with thermocouple to read the instant temperature of the furnace. It is also equipped with a water cooling system to keep the temperature low at the O-ring region when the furnace is heated to temperatures above 500^{o}C. Temperature of the holder is adjusted by changing the current flow into the furnace. The error in determining local sample temperature was +/- 25^{o}C.

TEM samples for *in-situ* ETEM experiments were prepared by gently crushing the catalyst sample between glass microscope slides and dispersing them onto a platinum (Pt) grid. Pt grids were chosen because of its chemical inertness even at high temperatures. The operating temperatures are well below the Tamman temperature of Pt, this keeps the diffusion of Pt atoms extremely low and likelihood of Pt interacting with the sample is

very small. To make sure the platinum grid is placed firmly onto the holder, two inconel washers were used on both sides of the grid and tightened with a hexring, both washers and the hexring are made of inconel.

2.5 Scanning Electron Microscopy

SEM is used to capture topological images of samples. Time consuming sample preparation is not needed while working with SEM. Larger and multiple samples can be placed on the sample stage compared to TEM. A SEM is composed of an electron column, scanning deflectors, several imaging detectors, and a control console. A SEM is similar to a STEM, except we collect reflected electrons rather than transmitted electrons, and there are no post-specimen lenses. Additionally, a SEM is operated at lower voltages of 1-30 keV typically, which increase the number of electron-sample interactions. The electron column contains an electron source, either a tungsten filament, lanthanum hexaboride (LaB_6) filament, or field emission source, and condenser lenses with deflectors to control the beam size and raster position. The control console has viewing screen and adjustment knobs such as brightness, contrast and astigmatism. A SEM collects secondary or backscattered electrons. Secondary electrons are emitted from the sample surface when beam electrons experience inelastic scattering events and eject low energy electrons. Backscattered electrons are those beam electrons that elastically reflect from the sample. Backscattered images have phase contrast and atomic number contrast. The area of interest in sample is scanned in lines by the beam controlled by a pair of deflectors. The magnification of the image is the ratio between length of the area projected on the screen to the length of the actual area scanned. When point to point electronic beam to sample interaction varies, contrast arises and thus the image is created.

The signal is created by the sample - electron interaction is accumulated by a detector, where the electrons are amplified by photomultiplier to be viewed on a cathode ray tube. A schematic diagram of a SEM is shown in Figure 2.4.

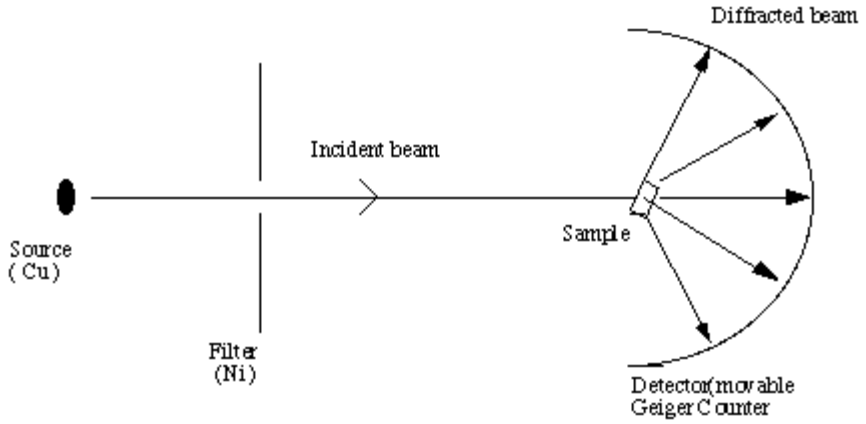

Figure 2.1. Schematic diagram[9] of a X-ray diffractometer. An electron beam hits a Cu source and generates X-rays. The X-rays are directed to a rotating sample, and the angles of diffracted intensity are recorded.

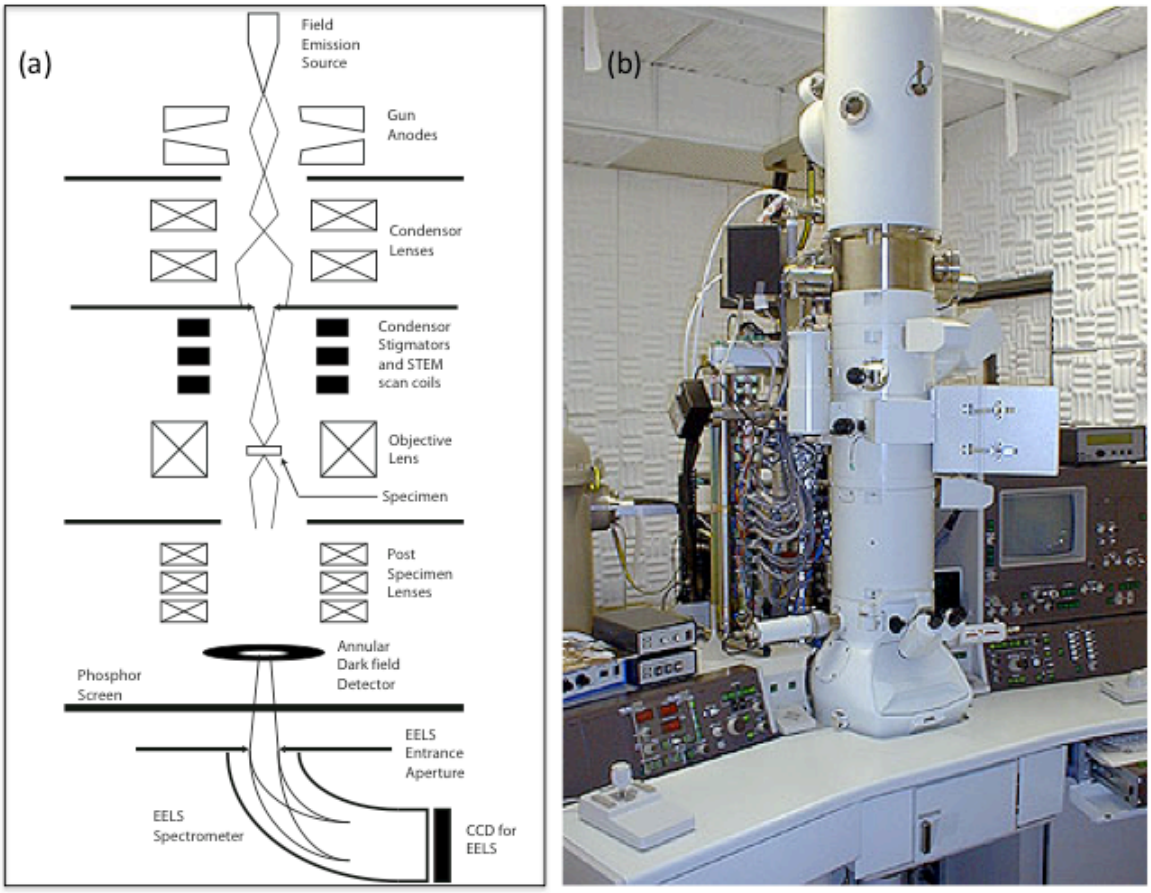

Figure: 2.2 (a) Schematic diagram[10] of a TEM/STEM including electron source, electromagnetic lenses, detectors, and EELS spectrometer. The sample sits inside the objective lens. (b) Photograph of a JEOL 2010F TEM/STEM[11] used in this thesis.

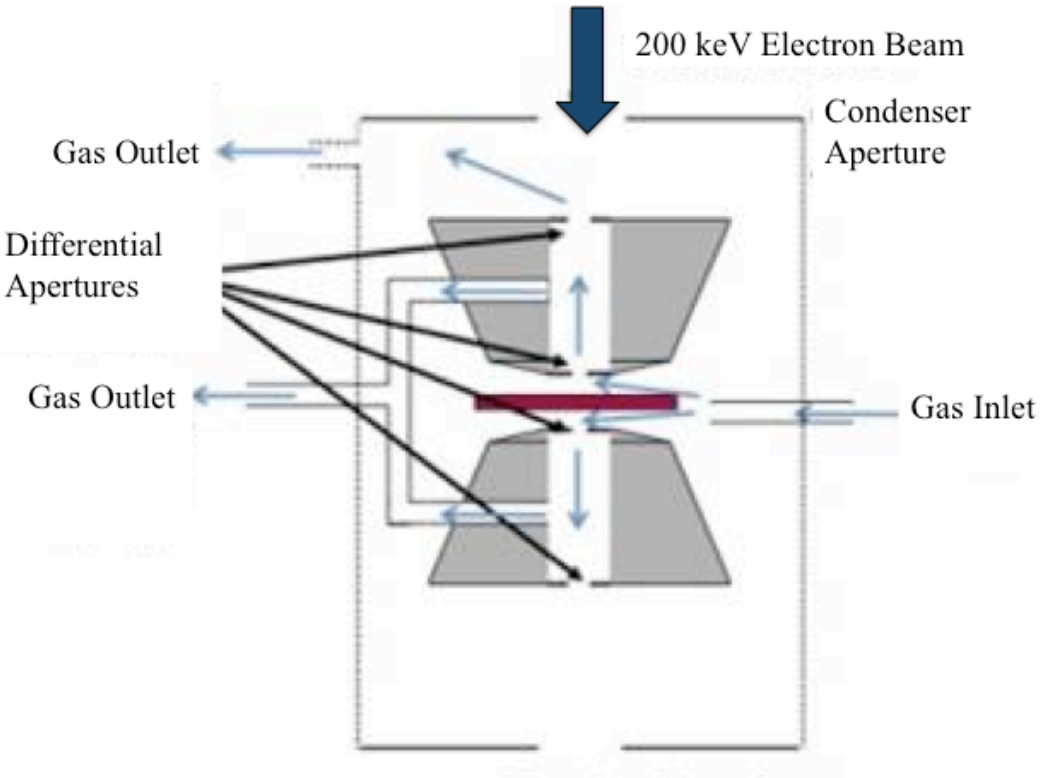

Figure 2.3. Schematic diagram[12] of differential pumping system in a TEM sample chamber.

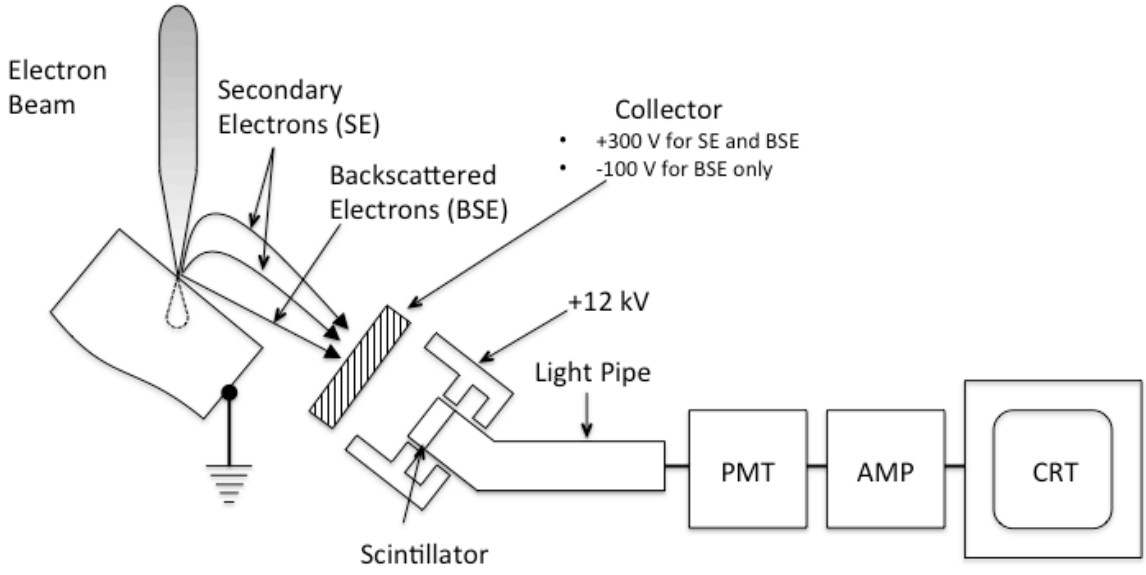

FIG. 2.4 Schematic diagram[6] of SEM. Secondary and backscattered electrons are collected to form images.

References

1. B. E. Warren. X-ray Diffraction. Addision-Wesley Publishing Company, Inc. Reading, Massachusetts, 1969.

2. B. D. Cullity. Elements of X-ray Diffraction. Addision-Wesley Publishing Company, Inc. Reading, Massachusetts. 1956.

3. D. B. Williams and C. B. Carter. Transmission Electron Microscopy: A Textbook for Materials Science. Plenum Press, New York, New York. 1996.

4. L. Reimer and H. Kohl. Transmission Electron Microscopy – Physics of Image Formation. Springer Science+Business Media, LLC. New York, New York. 2008

5. P. W. Hawkes, J. C. H. Spence. Science of Microscopy. Springer Science+Business Media, LLC. New York, New York. 2007.

6. J. Goldstein, D. Newbury, D. Joy, C. Lyman, P. Echlin, E. Lifshin, L. Sawyer, and J. Michael. Scanning Electron Microscopy and X-ray Microanalysis. Springer Science+Business media, Inc. New York, New York, 2003.

7. R. F. Egerton. Electron Energy-Loss Spectroscopy in the Electron Microscope. Springer Science+Business Media, LLC. New York, New York, 2011.

8. P. A. Crozier and S. Chenna. In situ Analysis of Gas Composition by Electron Energy-loss Spectroscopy for Environmental Transmission Electron Microscopy. *Ultramicroscopy* 111, 177 (2011).

9. S. Santra. Low Temperature Synthesis of ZnS and Mn Doped ZnS Quantum Dots. Thesis. Arizona State University, 2007.

10. A. B. Shah. Atomic Resolution Studies of Oxide Superlattices and Ultrathin Films. Dissertation. University of Illinois at Urbana-Champaign, 2010.

11. JEOL 2010F TEM/STEM. LeRoy Eyring Center for Solid State Science. Arizona State University. Downloaded 2014.

12. S. Chenna. In-situ Environmental TEM Studies For Developing Structure-Activity Relationship in Supported Metal Catalyst. Dissertation. Arizona State University, 2011.

Chapter 3

TiO_2 NANOTUBES SYNTHESIS, PHASE AND MORPHOLOGY STUDY

3. 1 Introduction

TiO_2 is an important photocatalyst that has attracted much attention for four decades. TiO_2 nanotubes in particular may yield enhanced catalytic activity as they provide a larger surface area and shorter electron-hole migration paths to the surface compared to other forms of TiO_2[1]. Anatase and rutile are two primary polymorphs, of which rutile is thermodynamically more stable in bulk form. Different phases and morphologies perform catalytically differently, which is discussed in chapter 1. In this chapter, we are discussing our work on phase and morphology study.

Phase transformation was studied in different forms of TiO_2 such as nanoparticles and nanotubes under different temperatures and gas environments[2-7]. In most of these works, X-ray diffraction (XRD) has been used as a major tool to identify the phases in the nanotubes. XRD provides the crystal structure averaged over a large number of nanotubes but does not yield information about the morphology. Here we employ both *ex-situ* and *in-situ* transmission electron microscopy (TEM) in addition to XRD and scanning electron microscopy techniques to determine structural and morphological evolution during thermally induced phase transformation in nanotubes.

While *ex-situ* studies yield information about phase and morphology of the tubes after heat treatments, *in-situ* TEM studies yield dynamic structural information of the tubes during the heat treatment. In this chapter, we have compared the morphology of *in-situ* with *ex-situ* experiments and analyzed the anatase to rutile transformation.

3.2 Tube preparation and formation Mechanism

Nanotubes were synthesized using an anodization technique, which involves an oxidation process followed by selective etching. Two types of tubes were synthesized - supported and freestanding as described below.

The supported nanotubes or aligned TiO_2 nanotube arrays supported on Ti metal were synthesized using an anodization method starting with a Ti foil (99.98% pure, Sigma Aldrich). Prior to tube synthesis, the Ti foil was mechanically polished followed by cleaning in acetone and ethyl alcohol. Aligned TiO_2 nanotubes were synthesized by anodization of Ti foils at 20 V for 5 hours in fluoride mediated ethylene glycol solvent, using a Pt foil as cathode. For a typical anodization experiment, 0.195 g of NH_4F was dissolved in 75 mL ethylene glycol solvent mixed with 3 mL of water. The experiment was conducted at constant voltage at room temperature. The as synthesized tubes were cleaned in deionized water to remove residual solvents. The supported tubes are open at one end with the other end terminating in the Ti metal foil.

To prepare freestanding nanotubes, thinner Ti foil was used of 12 μm thickness. Identical chemical composition and amounts were employed to synthesize the tube as above. A synthesis voltage of 60 V was applied in this reaction using the same chemicals for the electrochemical reaction. The reaction time was 5 hours and in this case the entire foil was etched, resulting in free standing tubes without any Ti metal support as seen in SEM images.

Several differences were observed between supported and freestanding nanotubes. The average diameter of the supported tubes was 40 nm, whereas the average diameter of the freestanding tubes was 100 nm (Figure 3.1a through 1d). The supported tubes were more

uniform in diameter and each tube was surrounded by an average of 6 tubes in an approximately hexagonal pattern with regularly occurring voids in between. The freestanding arrays of tubes are each surrounded by on average of 5 or 6 tubes with occasional voids between the tubes. The average length of the supported tubes and freestanding tubes are 2 μm and 12 μm, respectively. Supported tubes are closed at one end by Ti metal. Figure 3.2 shows a view along the supported tube length acquired in SEM. Length of the nanotubes was measured to be about 2 μm as seen in Figure.

The mechanism of tube formations via anodization process has been discussed in various literatures[6-10]. The oxidation process is initiated by reaction of the Ti^{4+} ion with O^{2-} ion in electrolyte. The fluoride ion present in the solution is responsible for selective dissolution of the oxide into the solution leaving the bare metal exposed for further oxidation. The two steps take place simultaneously to form the tube. The overall mechanism or the net reaction is expressed in the following set of chemical equations.

$$Ti\ (s) + 2H_2O\ (l) \rightarrow TiO_2\ (s) + 4H^+ + 4e^- \qquad (1)$$

$$TiO_2\ (s) + 6F^- + 4H^+ \rightarrow TiF_6^{2-}\ (aq) + 2H_2O \qquad (2)$$

Process (1) involves formation of oxide due to interaction of Ti metal surface with negative oxide ion from solution. In this process the anions move further towards metal/oxide surface while Ti^{4+} moves towards oxide/solution surface from metal. In the second step (2) two different processes help dissolving TiO_2. Field assisted and chemical (due to F anion) dissolution, out of which the former is dominating in initial phase[11] since a large electric field is created around the initially formed oxide layer. This leads to localized small pit formation. These pits grow into pores by moving down the layers. Both oxide formation and dissolution process occur at equal speed eventually, forming

well defined hexagonally patterned tubes. Hence the uniform tube formation is a time dependent evolution process. Each stage of the tube formation has been studied by SEM by Mor et al[10].

3.3 Synthesis parameters and their effect

To improve the nanotube qualities in terms of unidirectionality and uniformity of tube height, several experimental parameters were varied during the synthesis process.

3.3.1 Polishing

Polishing the Ti foil helped TiO_2 nanotubes grown more continuously on a smooth surface and the tubes were more uniform in terms of height and uniformity. The tubes synthesized on polished foil had a smoother surface, which yielded a more uniform electric field distribution over the metal surface[12]. Mechanical polishing was performed on the Ti metal foils. In a typical polishing procedure, a foil was polished on coarser to finer sand papers.

3.3.2 Voltage

The effect of voltage has been studied in nanotube formation, it has been seen that the tubes are of higher diameter and thickness when the working voltage is increased as shown in Table 3.1. It has been also studied[13] that the time taken for tube formation from stage of pore formation to tube formation as discussed in previous section is dependent on working voltage. As the working voltage increased, the time decreases.

3.3.3 Amount of etching agent

Varying the concentration of the fluoride ion was employed in order to determine the effect on the quality of the tubes. As shown in Figure 3.3, very high concentration of the

fluoride in solution makes the reaction more aggressive and oes not help the tubes to grow in a regular fashion[13].

3.3.4 Choice of conditions for nanotube synthesis

A voltage of 60 Vwas maintained throughout the growth on 0.25 mm thickness foil. For the thicker foil, 20V was determined as the best working condition. Different voltages were applied to synthesize tubes of various parameters and are summarized in Table 3.1

3.4 Phase and morphology study

3.4.1 *Ex-situ* study of transformations of tubes upon annealing

The as-prepared tubes are well aligned in one direction and have a narrow distribution of tube diameters with an average value of approximately 100 nm. Figure 3.4 (b-d) shows SEM images of tubes annealed *ex-situ* in one atmosphere of air for 2 hours at 450, 600, and 800 °C respectively.

The tubes annealed at 450 °C appear to be intact, however at 600 °C the tubes are less well defined and the morphology suggest signs of damage to the tubular structure. By 800 ^{o}C there is no tubular structure observed in the SEM image.

Figure 3.5 shows XRD data of the tubes annealed at different temperatures. Peaks are labeled as A, R and T for anatase, rutile and titanium metal (from the Ti substrate used for anodization) respectively. The as-prepared tubes are amorphous and only the Ti signal was seen coming from the underlying metal substrate, whereas the tubes annealed at 280 ^{o}C and 450 ^{o}C are predominantly anatase. Both anatase and rutile phases exist at 600 ^{o}C and complete transformation to rutile takes place at 800 ^{o}C. To obtain information on amorphous and crystalline domains in different areas, transmission electron microscopy

was performed on nanotubes that were annealed at 280 ^{o}C for 2 hours and 8 hours. A representative high resolution TEM image of a TiO_2 nanotube annealed at 280 ^{o}C is shown in figure 3.6a along with the Fast Fourier transform (FFT) from two selected regions of the image. FFT's from two regions show that the nanotube consists of both amorphous and crystalline structures. Figure 3.6b and 3.6c show the magnified areas from figure 3.6a. Figure 3.6b shows the characteristic salt and pepper contrast indicative of amorphous structure. Figure 3.6c shows lattice fringes indicating crystallinity in this region and the lattice spacing was measured to be 0.35 nm that matches with the anatase (101) d-spacing. Thus for this sample the TEM images show that amorphous regions are mixed with crystalline regions at the nanometer level. Figure 3.6d shows a corresponding selected area diffraction pattern taken from the same group of tubes. The pattern shows a small number of Bragg reflections in addition to several diffuse rings. This indicates the presence of a few crystalline grains embedded in an amorphous matrix. (The selected area aperture was placed over areas, which did not include the amorphous carbon support film in order to avoid the overlap).

Figure 3.7 shows a TEM image of a nanotube that was annealed *ex-situ* at 450 ^{o}C. The TEM image shows a quasi-facetted void structure in the tube wall. The TEM image is consistent with the SEM image of Figure 3.4b but the TEM analysis shows that the tube morphology has undergone significant disruption. While the facets are not perfectly straight they are not random and the angle between the planes making up the sides of the void is approximately 120^{o}. The lattice plane parallel to one side of the void has a spacing of 2.36 Å, which matches the (112) planes of anatase. For anatase, the other

primary plane making an angle of 119^{o} with respect to the (112) are the (004) planes. Thus the voids are composed of (112) and (004) rough facets.

Upon analyzing the high-resolution images of tubes annealed at 450 ^{o}C, it was noticed that there were small domains of rutile along with anatase as shown in figure 3.8 (a). Figure 3.8(b) is an FFT acquired from this image showing diffraction spots corresponding to anatase (101) and rutile (110) planes. Figure 3.8(c) shows overlaid and colorized digital dark-field images obtained by selecting only the anatase or rutile reflections and performing an inverse Fourier transform. The average size of such rutile domains was found to be 12 nm. Figure 3.8(e) is the selected area electron diffraction pattern which also shows the rutile (110) reflection in addition to the anatase reflections. There is a 10% increase in the density between anatase and rutile (density of anatase and rutile are 3894 and 4250 kgm^{-3} respectively), which would impose substantial stress on the nanotube structure during the phase transformation contributing to destabilization and destruction of the tubular structure. In the work by Fang et al[14] they reported a shortening of the tube length upon annealing to 600 ^{o}C due to the anatase-to-rutile transformation and resulting density increase. They also showed TEM images, though not discussed in detail, with faceted voids formation in the tube walls after annealing at 450 ^{o}C.

3.4.2 *In-situ* transformations

In-situ heating was performed in the ETEM to understand the mechanism for the morphological and structural changes with temperature. Figure 3.9 (a-e) shows the *in-situ* ETEM images of nanotubes in the presence of 1 Torr of air heated from room temperature to 650 ^{o}C. Two arrows are guides to follow the morphological evolution of

the nanotube surface with respect to temperature. The nanotube has a single continuous wall at room temperature, and no significant change was observed up to 450 ^{o}C. At 550 ^{o}C, the surface of the nanotubes becomes rough and the dark line associated with the inner wall of the tubes shows discontinuities at certain places indicating that the tube structure is starting to disintegrate. By 650 ^{o}C, the nanotube wall was no longer continuous and was composed of nanoparticles 30-60 nm in size. These nanoparticles appeared to nucleate along the length of the tube and essentially consume the wall material during the disintegration.

The nanotube morphology was monitored up to 800 ^{o}C. Figure 3.10a shows an *in-situ* TEM image of the TiO_2 nanotube heated to 800 ^{o}C in 1 Torr of air. From the image it is clear that the nanotube was completely transformed to nanoparticles 50-100 nm in size. There is some residual directionality in the alignment of the nanoparticles along the original tube direction but the tube structure is completely destroyed. Figure 3.10b shows a TEM image of the TiO_2 nanotubes at 800 ^{o}C in the presence of 1 Torr of air. The lattice spacing was measured to be 0.35 nm, which corresponds to anatase (101). No grains of rutile were observed at 800 ^{o}C throughout the specimen. Figure 3.10c is the *in-situ* electron diffraction taken at 800^{o}C in 1 Torr of air, which also shows that the diffraction pattern matches with that of anatase. This is in contrast to our *ex-situ* experiments performed at 760 Torr air, in which grains of rutile formed at 600 ^{o}C and the sample was completely transformed to rutile by 800^{o}C.

Electron energy-loss spectroscopy (EELS) was also acquired to confirm the identification of different phases of tubes. The fine structure in the oxygen K-edge is sensitive to electronic structure in TiO_2 polymorphs, which can be used to identify the phase of the

TiO_2[15]. EELS spectra were acquired from synthesized tubes that are purely amorphous, and the annealed tubes with mixed phases of anatase and amorphous. EELS reference spectra were also acquired from commercially available anatase and rutile powders. Figure 3.11 shows the O K-edge EELS spectra from different TiO_2 nanotubes and the reference titanias , which matched those available in literature[19]. Figure 3.12, shows the O K-edge from TiO_2 nanotube in the presence of 1 Torr of air at 800 ^oC. The energy-loss spectrum clearly matches with that of the anatase structure (shown in figure 3.11) and this once again confirms that the nanoparticles are anatase.

To validate the *in situ* experiments, we also performed *ex-situ* heating on unsupported nanotubes to determine if the low oxygen pressure or Pt grid material for the *in situ* experiment influenced the structural evolution of the tubes. Figure 3.13 shows an HRTEM image, SAD pattern, along with an energy-loss spectrum (Figure 3.14) recorded from unsupported nanotubes heated in air to 800 ^oC and then transferred to the microscope for observation at room temperature. A plane spacing from HRTEM and SAD was measured to be 0.35 nm corresponding to the (101) Miller planes of anatase. Moreover, the near edge structure of the oxygen K-edge in the EELS matches the anatase phase. This *ex situ* experiment proves that the Pt grid material did not influence the *in situ* experiment and that changing the oxygen partial pressure from 0.2 – 160 Torr does not significantly influence the phase transformation.

It was interesting to see the predominant anatase phase in unsupported nanotubes at 800 ^oC during the *in-situ* and *ex-situ* heating in air. These experiments show that anatase is retained up to 800 ^oC over a significant range of oxygen partial pressure. However, when nanotubes are supported however they transform to rutile at approximately 450 ^oC. It has

been reported that the anatase to rutile transformation in TiO_2 depends on the annealing environment conditions including annealing temperature, and presence of dopants present in TiO_2.[16] In one hypothesis, the transformation is facilitated by the density of oxygen vacancies in the initial anatase. Since the anatase to rutile transformation is reconstructive[16], which involves bond breaking and reforming, the relaxation of the oxygen sublattice due to oxygen vacancies reduces the overall structural rigidity and hence facilitates the anatase-to-rutile transformation[17-18]. In our case, the oxygen partial pressure for the *ex-situ* experiment is 160 Torr compared to 0.21 Torr for the *in-situ* experiment. If the lower oxygen partial pressure resulted in a significant increase the concentration of oxygen vacancies in the anatase it should trigger the rutile phase transformation at lower temperature. We observe the opposite behavior suggesting that the pressure difference is not the origin for the differences observed between the *in-situ* unsupported tubes and *ex-situ* supported tubes results.

There have been considerable variations in the reported phase stability of anatase during thermal treatments of titania nanotubes. Recent work by Fang showed that supported and unsupported tubes behave very differently during thermal treatment[14]. For titania nanotubes supported on titanium metal substrate, they found that annealing at 450 ^{o}C gave predominantly anatase and annealing at 750 ^{o}C gave rutile. This is consistent with our *ex-situ* observation showing the onset or rutile formation at 450 ^{o}C and complete transformation to rutile by 800 ^{o}C. For unsupported tubes they found that anatase was the stable phase up to 800 ^{o}C and that the transformation to rutile took place at 900 ^{o}C. Again this is also in agreement with our observations. To prepare the TEM sample, we effectively scrape the titania nanotubes off the titanium metal substrate. This means the

nanotubes in the ETEM experiment are unsupported. Our observation is that they remain anatase even up to 800 ^{o}C in agreement with the work of Fang. Other groups have recently observed a suppression of the anatase to rutile phase transformation on unsupported titania nanotubes[19].

The issue of the thermodynamic origins of anatase phase stability in nanoscale titania has been explored by several authors over the last decade. While bulk thermodynamics shows that rutile is the more stable phase, for nanomaterials the contribution of the surface energy has to be taken into account to give a correct description of the thermodynamic behavior. The surface energy of anatase was found to be much lower than that of rutile for spherical particles less than 66 nm and thermodynamic calculations suggest that anatase should be more stable than rutile. In our case, the nanotube wall thickness is around 10 nm so certainly the low surface energy of the anatase tube will inhibit the phase transformation to rutile at lower temperature before significant coarsening occurs. By 800 ^{o}C, most of the tube wall has been destroyed and replaced with nanoparticles of titania which have undergone significant coarsening and are in the size range 50-100 nm. Further heating would result in additional coarsening and eventually the difference in free energy of the bulk phases will dominate the energetics and these larger nanoparticles will transform to rutile.

For the supported nanotubes (in this case the nanotubes that were heat treated under *ex-situ* conditions), the phase change is believed to occur at lower temperature because of the influence of the metal/ceramic interface on the local oxygen vacancy concentration. Rutile seems to form more easily at the base of the nanotube that is in contact with the Ti metal substrate[20]. These rutile crystals grow during annealing and consume the larger

anatase crystals. During annealing, the anatase crystallites in the walls of the tube coarsen and the difference in energy between the anatase and rutile phases becomes less. When the anatase crystal comes into contact with the rutile crystal they get consumed. For the unsupported tubes (in this case the nanotubes that were heat treated under *in-situ* conditions), TiO_2/Ti interface is absent in this case and the rutile nucleation is inhibited which explains the absence of rutile phase even at 800 ^oC in case of *in-situ* heat treatment.

3.5 Summary

Ex-situ and *in-situ* TEM studies were performed on TiO_2 nanotubes synthesized via an anodization method. The effect of heat treatment on both the phase and morphology was investigated under different conditions. From the *ex-situ* studies, the amorphous nanotubes start to transform to anatase at 280 ^oC in the presence of 1 atm. At 450 ^oC, XRD data showed the tubes to be predominantly anatase, however from the high-resolution TEM analysis, small domains of rutile were observed in addition to the anatase. Complete transformation of anatase to rutile took place at 800 ^oC. In contrast to *ex-situ* data, *in-situ* TEM studies (in the presence of 1 Torr of air) did not show any formation of rutile even at 800 ^oC. In *ex-situ* heat treatment, the nanotubes were supported on the Ti foil and the presence of the metal/ceramic interface influenced the local oxygen vacancy concentration facilitating the formation of rutile phase. In *in-situ* heat treatment, the nanotubes are free standing and do not form the rutile phase. In both cases, the morphology of the nanotubes changes drastically from a tubular structure to tubular aggregates of individual nanoparticles. For the supported tube, morphology

change was initiated by the formation of rutile followed by coarsening whereas for the unsupported tubes, coarsening (to lower the surface energy) was the main mechanism for tube destruction.

Table 3.1 Influence of voltage on TiO_2 tube parameters

Applied Voltage (V)	Inner Tube Diameter (nm)	Outer Tube Diameter (nm)	Wall Thickness (nm)
10	28	44	8
20	46	79	16
40	100	140	20
60	117	163	23

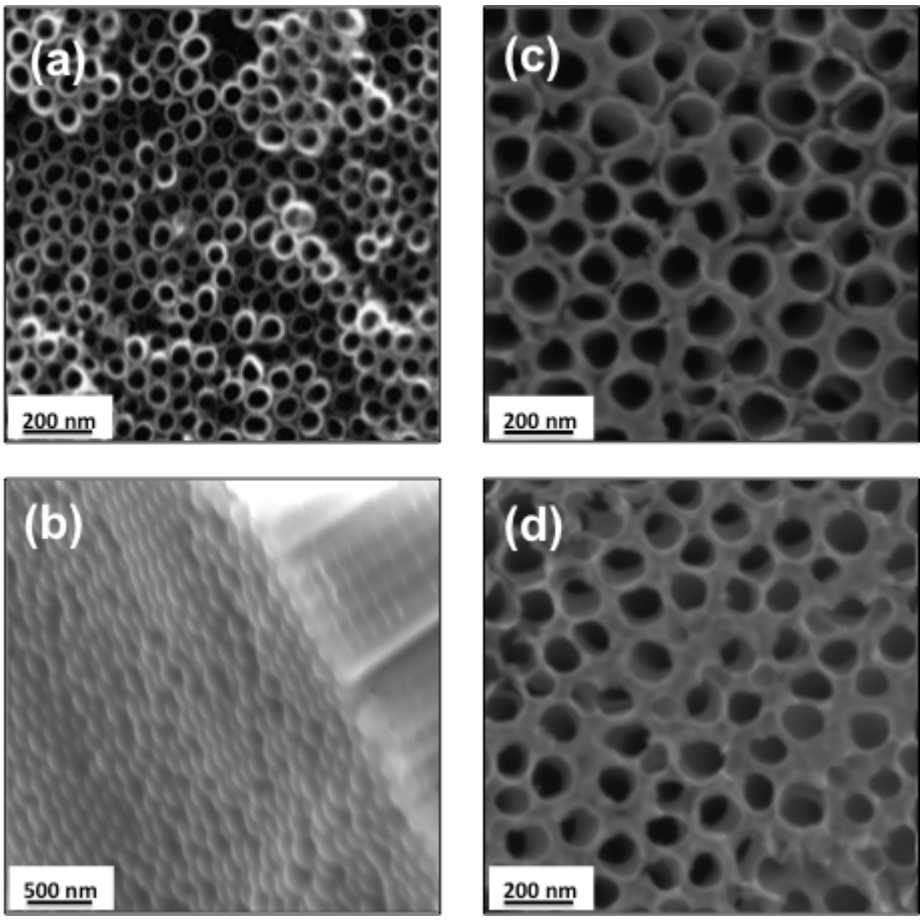

FIG. 3.1. SEM images of (a) supported TiO_2 nanotubes showing the open end (b) closed end of the same tubes after removal from the Ti metal support (c) one end of the free standing tubes (d) other end of the free standing tubes.

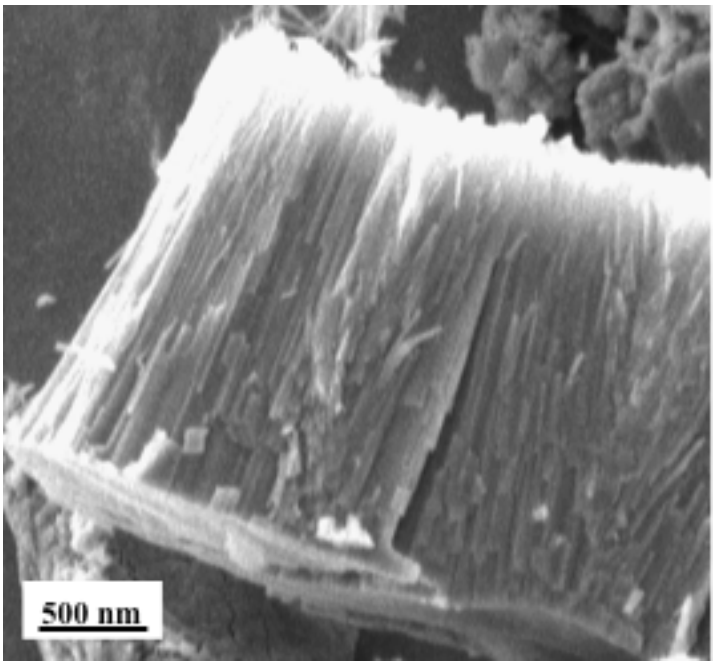

FIG. 3.2. SEM image of TiO_2 nanotubes showing the length of the nanotubes of about 2 micron.

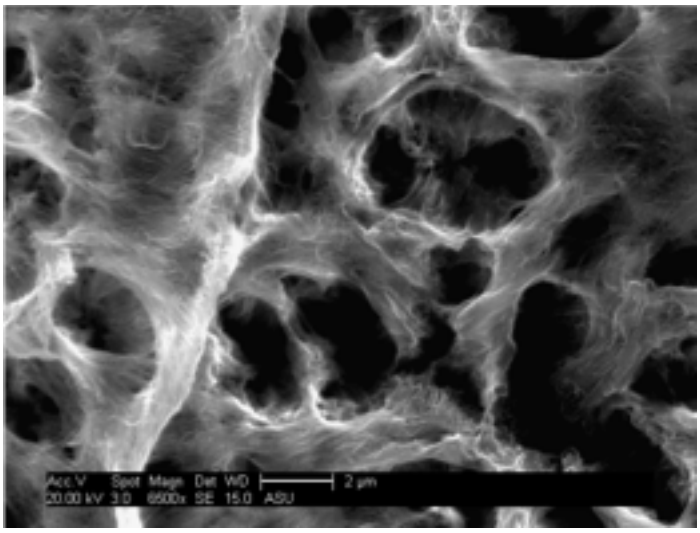

FIG. 3.3. SEM image of TiO_2 nanotubes grown in excess etching agent, showing tubes grown in random direction.

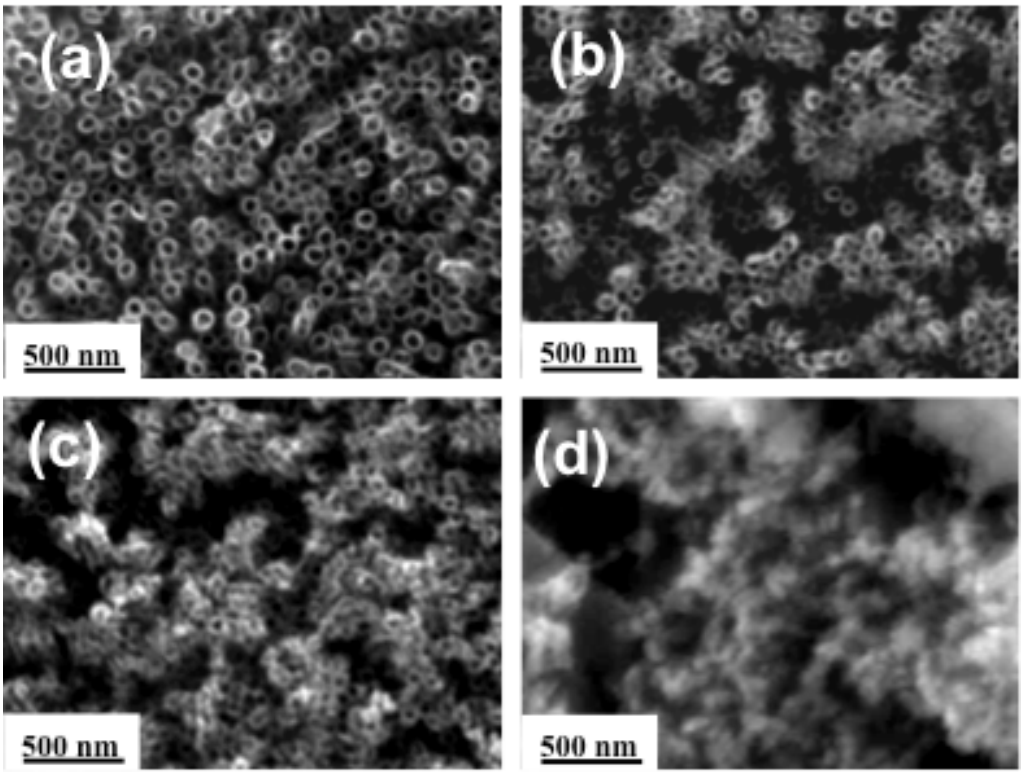

FIG. 3.4. SEM images of (a) as-prepared TiO_2 nanotubes, tubes heat treated at (b) 450 ^oC , (c) 600 ^oC (d) 800 ^oC

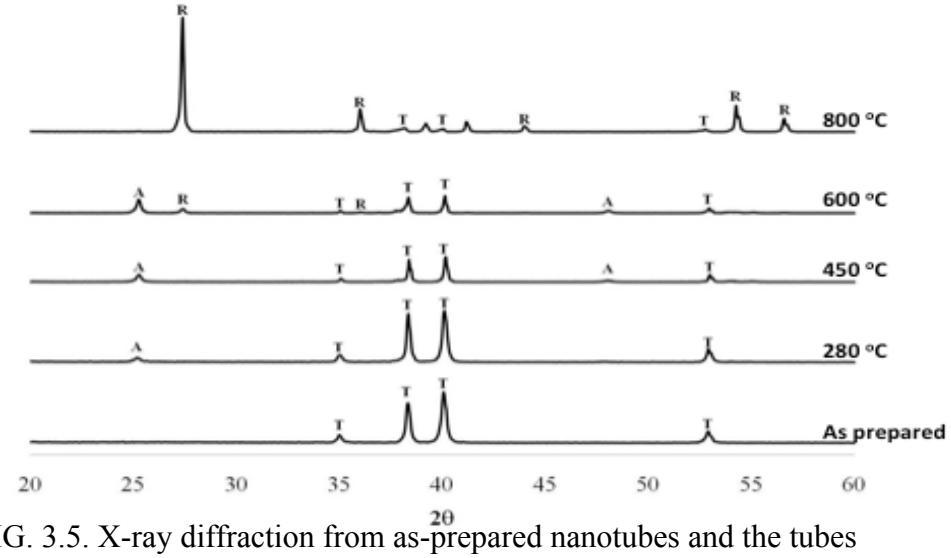

FIG. 3.5. X-ray diffraction from as-prepared nanotubes and the tubes annealed at different temperatures.

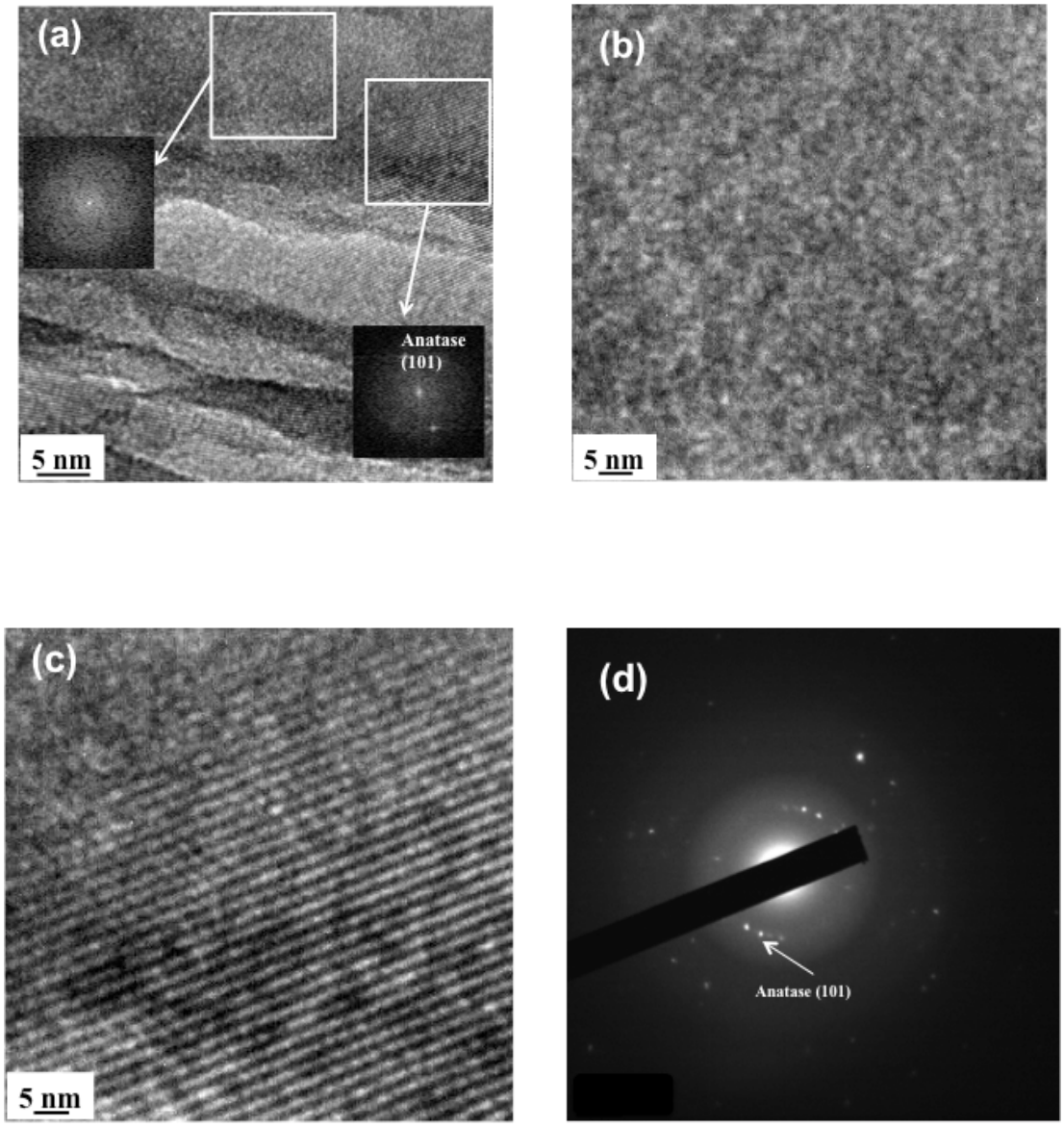

FIG. 3.6. (a) TEM image of nanotubes annealed at 280 °C for 2 hours showing amorphous regions in panel (b) crystalline anatase phase in panel (c) and (d) corresponding electron diffraction pattern, (101) plane = 0.35 nm d spacing.

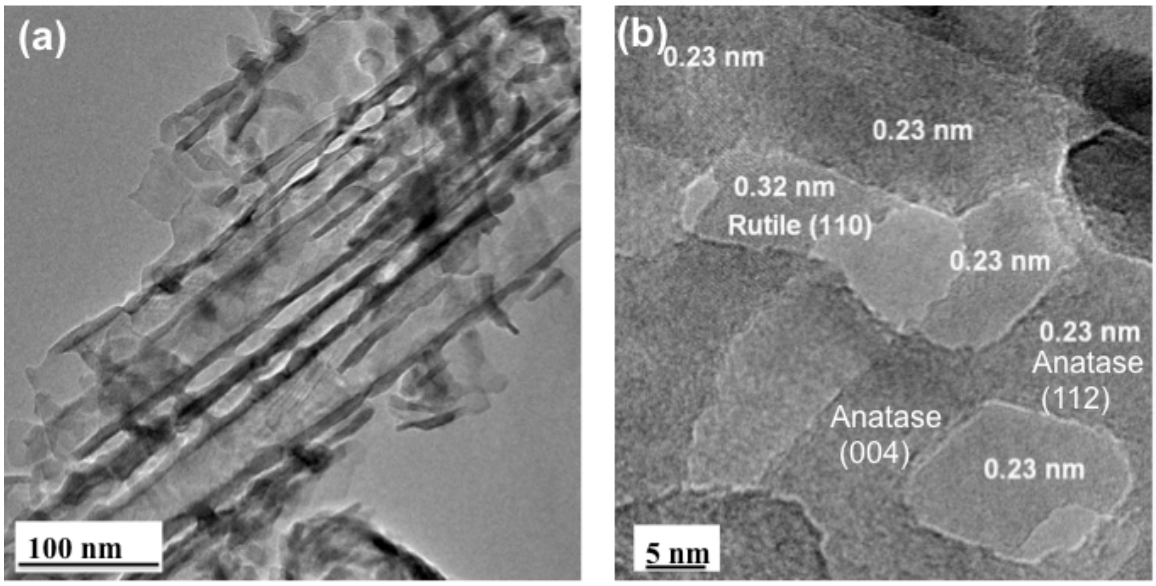

FIG. 3.7. Ex-situ TEM image of TiO_2 nanotube after annealing at 450 ^oC (a) at low magnification (b) showing the presence of faceted voids in the TiO_2 nanotube.

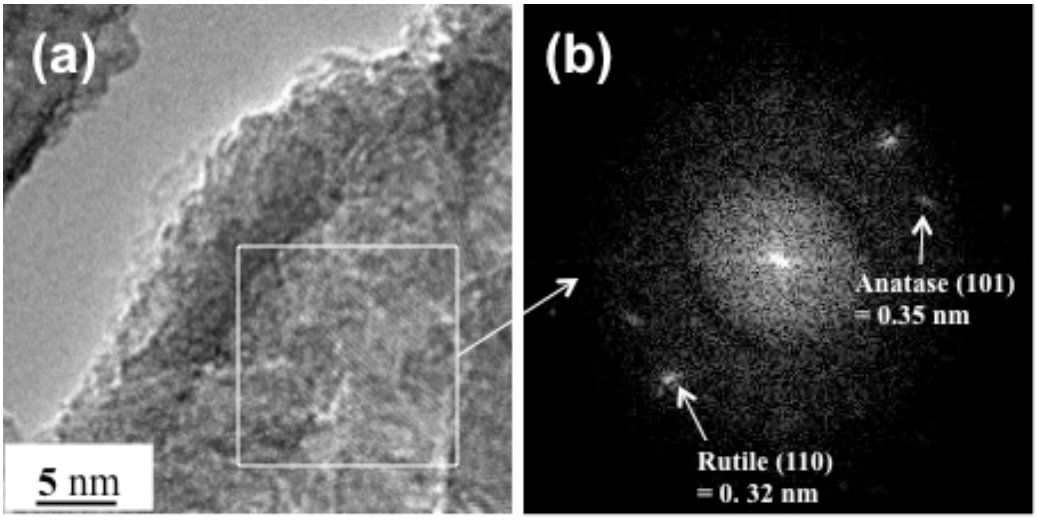

FIG. 3.8 (a) High resolution TEM image of tube annealed at 450 ^oC (b) FFT from the image (c) Colorized presentation of selected area - blue represents anatase and red the rutile phase (d) original image of colorized version (e) representative selected electron diffraction of tubes annealed at 450 ^oC, showing anatase reflections (101), (004) corresponding to d-spacings 0.35 and 0.23 nm; rutile reflections (110) and (200) corresponding to 0.32 and 0.22 nm respectively.

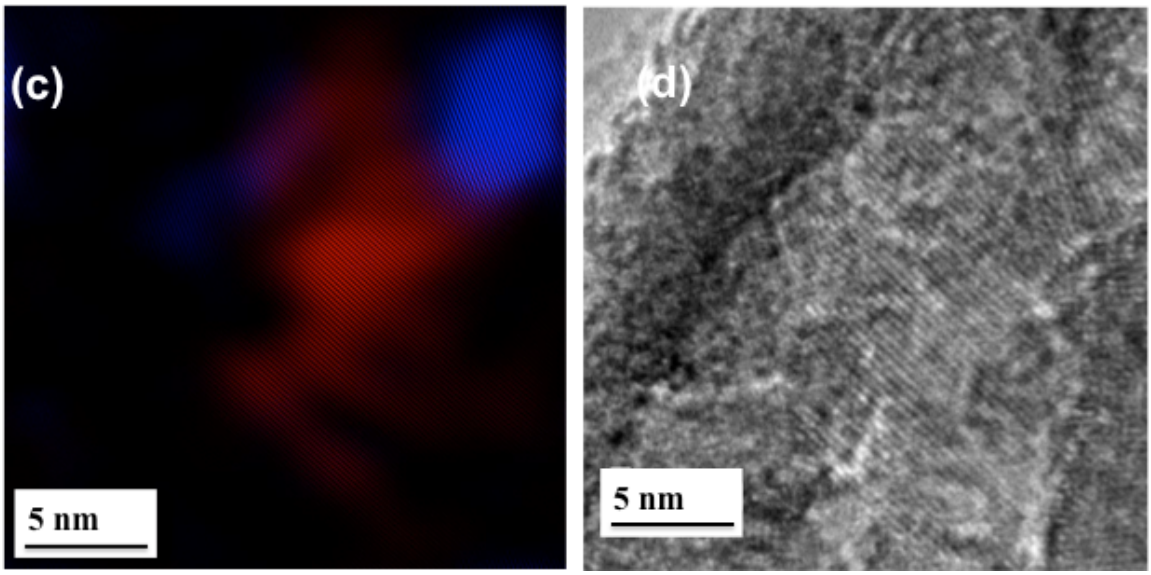

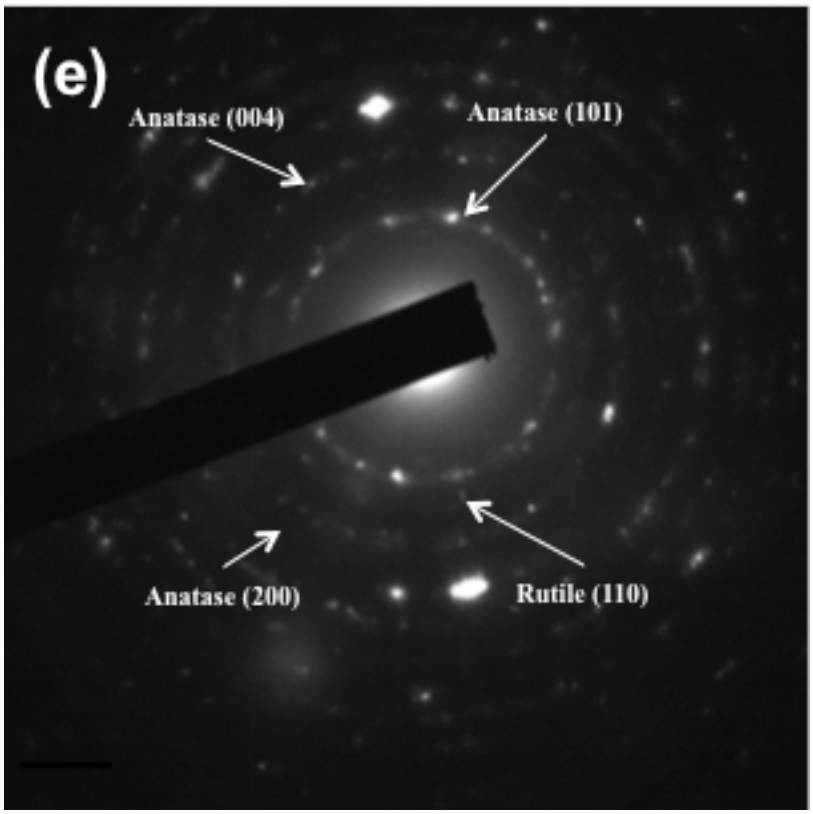

FIG. 3.8 (c) through (e)

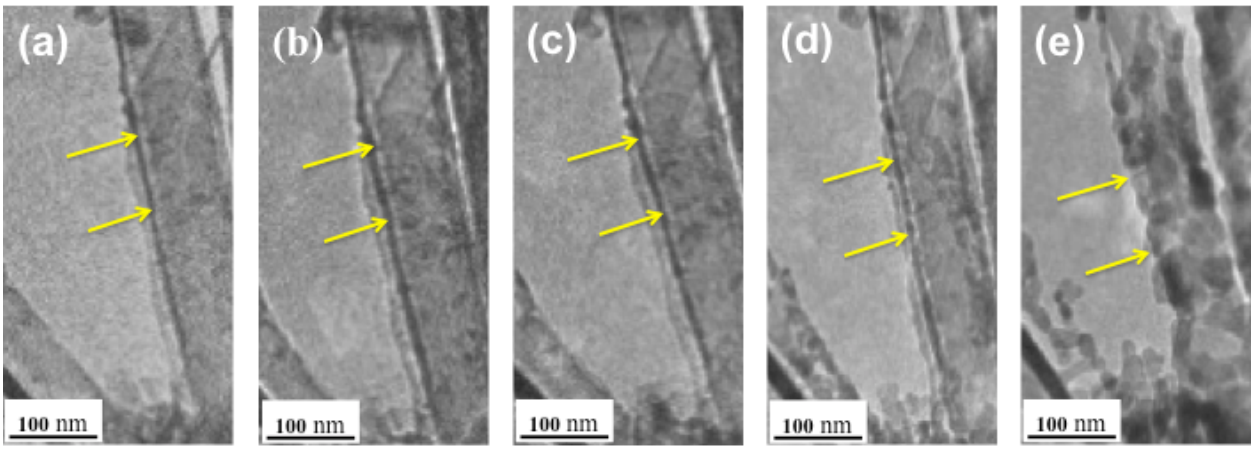

FIG. 3.9. *In-situ* TEM image of the evolution of nanotubes with increase in temperature, (a) room (b) 280 ^{o}C (c) 450 ^{o}C (d) 550 ^{o}C and (e) 650 ^{o}C

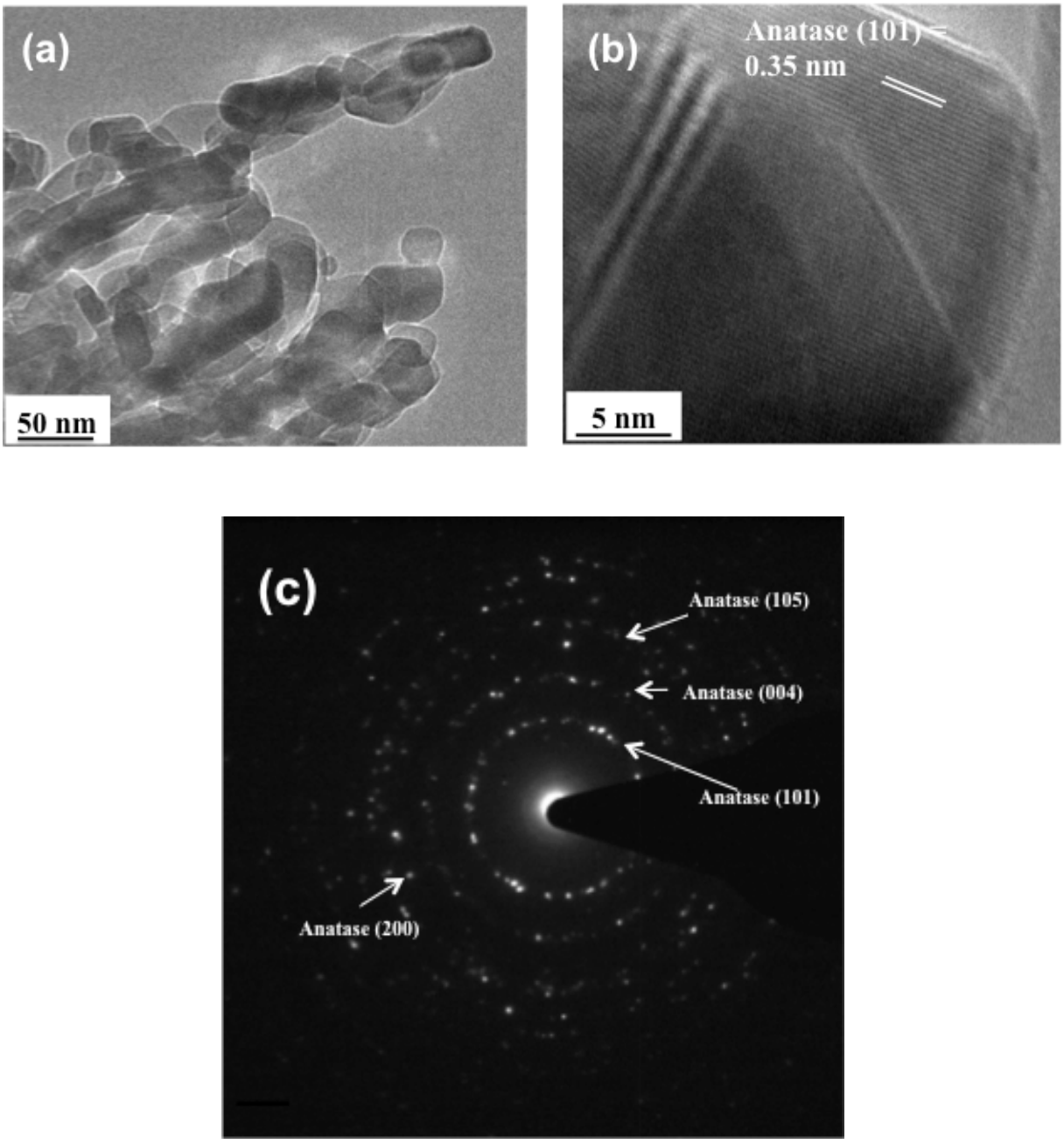

FIG. 3.10. (a) *In-situ* TEM image of the nanotube at 800 ^{o}C. (b) Representative HRTEM image of several grains and (c) corresponding electron diffraction showing anatase reflections (101), (004), (200) and (105) corresponding to d-spacings 0.35, 0.23, 0.18 and 0.16 nm respectively.

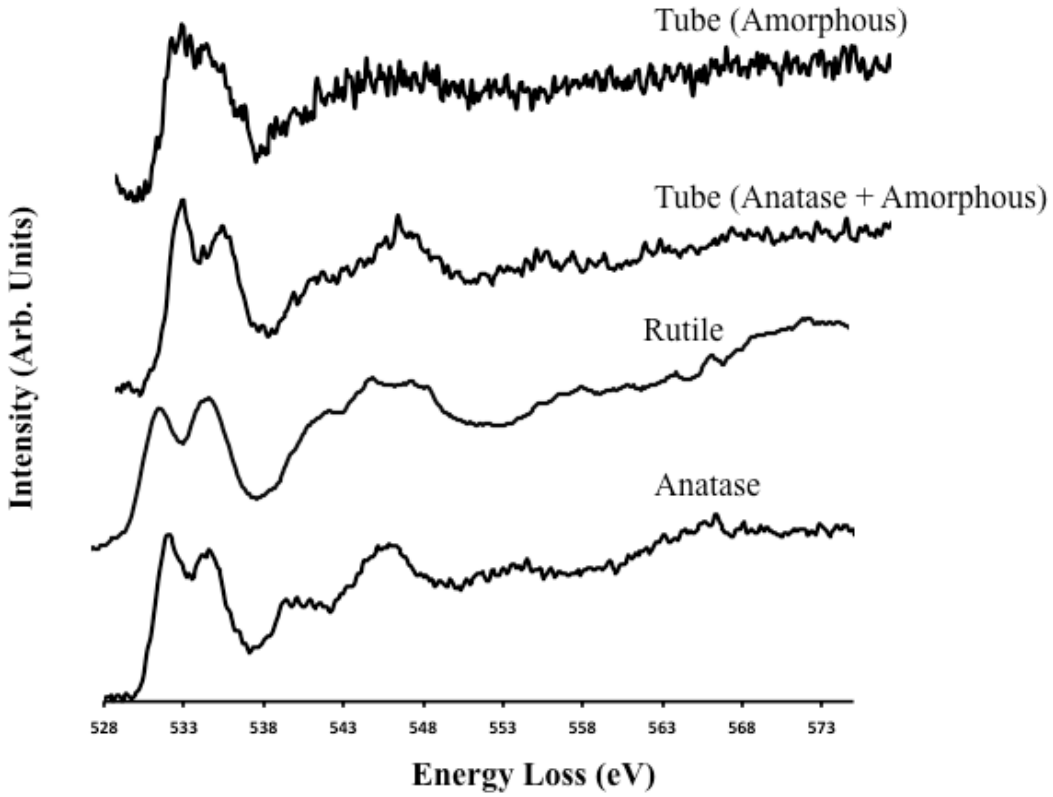

FIG. 3.11. Electron energy-loss spectra showing the O K-edge from different TiO_2 phases.

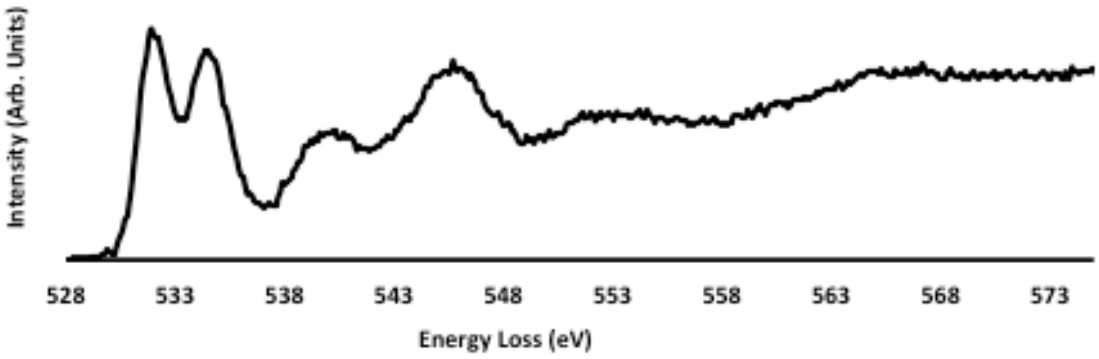

FIG. 3.12. *In-situ* electron energy-loss spectrum from TiO_2 nanoparticles in the presence of 1 Torr of air at 800 ^{o}C.

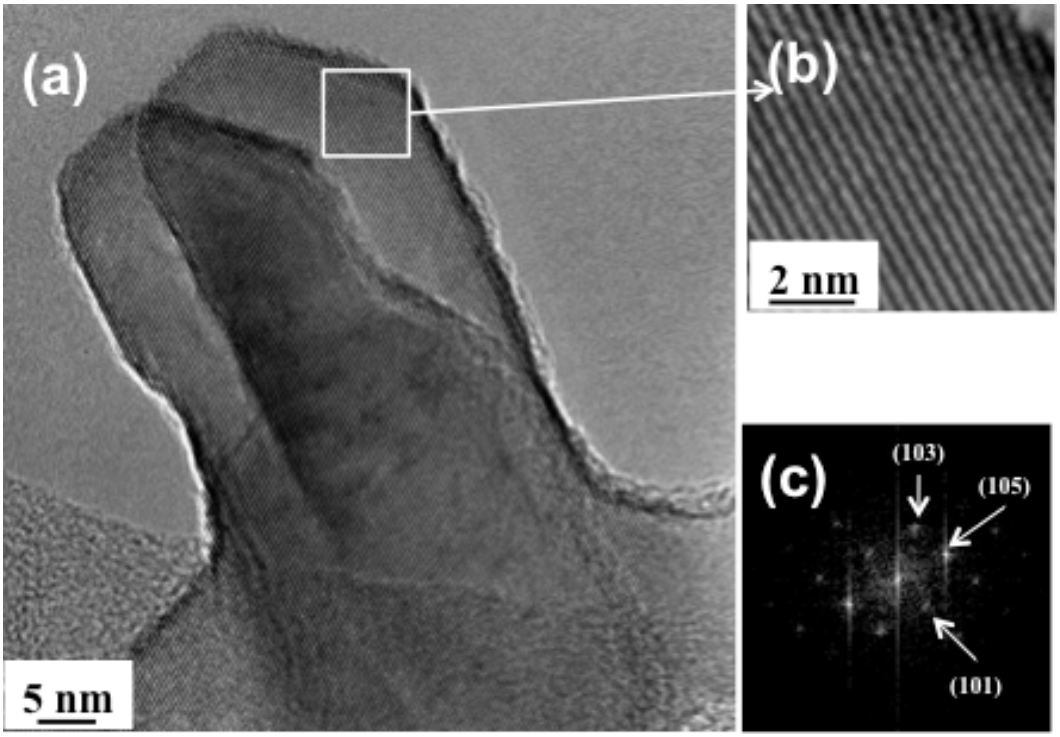

FIG. 3.13. (a) High-resolution TEM image TiO_2 nanoparticles that was formed after heat treating unsupported TiO_2 nanotubes at 800 ^{o}C under ex-situ conditions. (b) and (c) showing the zoomed in image and the corresponding FFT showing the anatase

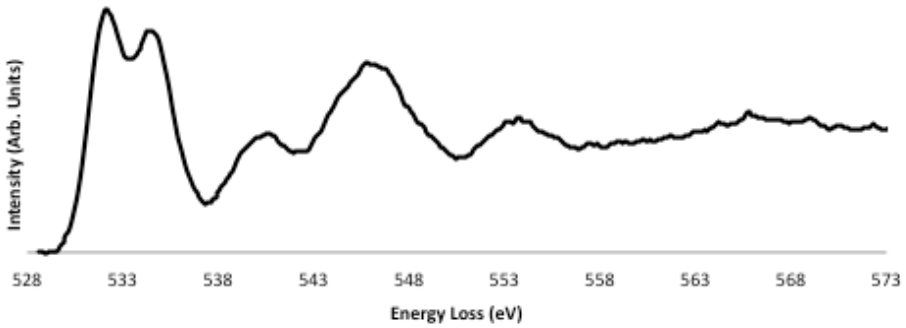

FIG. 3.14. Electron energy-loss spectrum from TiO_2 nanoparticles that was formed after heat treating unsupported TiO_2 nanotubes at 800 ^{o}C under ex-situ conditions.

REFERENCES

1. M. Adachi, Y. Murata, M. Harada, and S. Yoshikawa: Formation of titania nanotubes with high photocatalytic activity. *Chem. Lett*. **29**, 942 (2000)
2. M. P. Neupan, S. Park, M. H. Lee, T S Bae and F. Watari: Influence of heat treatment on morphological changes of nano-structured titanium oxide formed by anodic oxidation of titanium in acidic fluoride solution. *Bio-Med. Mater. Eng*.**19**, 77 (2009)
3. V. K. Mahajan, M Misra, K S Raja and S K Mohapatra: Self-organized TiO_2 nanotubular arrays for photoelectrochemical hydrogen generation: effect of crystallization and defect structures. *J. Phys. D: Appl. Phys*. **41**,125307 (2008)
4. Y. Chen, K. S. Kang, K. H. Yoo, N. Jyoti, and J. Kim: Cause of Slow Phase Transformation of TiO_2 Nanorods. *J. Phys Chem. C Lett*.**113**, 19753 (2009)
5. Y. Gao, Y. Masuda, W-S. Seo, H. Ohta and K. Koumoto: TiO_2 nanoparticles prepared using an aqueous peroxotitanate solution. *Ceram. Int*. **30,** 1365 (2004)
6. Y. Liao and W. Que: Preparation and photocatalytic activity of TiO2 nanotube powders derived by a rapid anodization process. *J Alloys Compd*. **505,** 243 (2010)
7. A. Nakaruk, D. Ragazzon and C.C. Sorrell: Anatase–rutile transformation through high-temperature annealing of titania films produced by ultrasonic spray pyrolysis. *Thin Solid Films*. **518**, 3735 (2010)
8. S.H. Kang, J-Y Kim, H. S. Kim, Y.-E Sung: Formation and mechanistic study of self-ordered TiO_2 nanotubes on Ti substrate. *J. Ind. Eng. Chem.* **14**, 52 (2008)

9. S. Joo, I. Muto, N. Hara: In Situ Ellipsometric Analysis of Growth Processes of Anodic TiO_2 Nanotube Films. *J. Electrochem. Soc.* **155**, C154 (2008)

10. G.K. Mor, O.K. Varghese, M. Paulose, N. Mukherjee, C. A. Grimes: Fabrication of Tapered, Conical-shaped Titania Nanotubes. *J. Mater. Res.* **18**, 2588 (2003)

11. B.J. Hwang, J.R. Hwang: Kinetic-model of anodic-oxidation of titanium in sulfuric acid. J. Appl. Electrochem. **23,** 1056 (1993)

12. Y. Shin and S. Lee: Self-Organized Regular Arrays of Anodic TiO_2 Nanotubes. *Nano Lett*. **8,** 3171 (2008)

13. Y. Alivov, M. Pandikunta, S. Nikishin, Z.Y. Fan: The anodization voltage influence on the properties of TiO_2 nanotubes grown by electrochemical oxidation. Nanotechnology. **20,** 225602 (2009)

14. D. Fang, Z. Luo, K. Huang and D.C. Lagoudas: Effect of heat treatment on morphology, crystalline structure and photocatalysis properties of TiO_2 nanotubes on Ti substrate and freestanding membrane. *Appl Surf Sci.* **257** 6451 (2011)

15. A. Gloter, C. Ewels, P. Umek, D. Arcon, and C. Colliex: Electronic structure of titania- based nanotubes investigated by EELS spectroscopy. *Phys Rev B*. **80**, 035413 (2009)

16. D. A. H. Hanaor and C.C. Sorrell: Review of the anatase to rutile phase transformation. *J Mater Sci*. **46**, 1 (2011)

17. R.D. Shannon and J.A. Pask: Kinetics of anatase-rutile transformation. *J Am Ceram Soc*. **48**, 391 (1965)

18. J. A. Gamboa and D. M. Pasquevich: Effect of chlorine atmosphere on the anatase-rutile transformation. *J Am Ceram Soc*. **75**, 2934 (1992)

19. J. Liao, S. Lin, N. Pan, S. Li, X. Cao and Y. Cao: Fabrication and photocatalytic properties of free-standing TiO_2 nanotube membranes with through-hole morphology *Mater. Charact.* **66,** 24 (2012)

20. O. K. Varghese, D. Gong, M. Paulose, C. A. Grimes and E. C. Dickey: Crystallization and high-temperature structural stability of titanium oxide nanotube arrays *J. Mater. Res.* **18,** 156 (2003)

Chapter 4

METAL FUNCTIONALIZATION OF TiO_2 NANOTUBE

4.1 Introduction

Metal nanoparticles have been loaded on TiO_2 powders and other supports for catalytic applications[1-2] but efficient functionalization of tubes with nanoparticles is challenging because of the tube shape and stability. For photocatalytic applications, the tubes should ideally be functionalized with a uniform distribution of small metal particles along a length comparable to the light penetration depth. As discussed in chapter 1, photoreduction is a suitable technique for functionalization to avoid post heat treatments. Among different metals photodeposition experiments; Ag, Au, Rh, Pt metals were deposited on supports such as powders[3-8], rods[9-10], substrate[11], wire[12], and colloids[13]. Again, deposition of these systems only involved the outer surface, and is easier in comparison to the tube systems. Since arrays of tubes are closed at one end and most of the free surface area available is inside the tubes, it is important to functionalize the inner surface of the tubes. Photodeposition has been employed far less in tubes. For TiO_2 nanotubes, metal should only be deposited along the tube to a depth comparable with the photon penetration depth. Moreover, the metal particles will nucleate at points on the titania surface where photoelectrons reach the surface. This corresponds to catalytically active locations in the titania where electron hole pair separation is suppressed and efficient charge transfer to the surface can occur. Tian et al.[14] functionalized Pt nanoparticles on TiO_2 nanotubes in a two-step process first to obtain a dendrimer structure followed by an electrochemical treatment to obtain partial conversion to small

particles. In more recent works[15-16], Ag metal was photodeposited on TiO_2 nanotubes, in two steps; however the resulted particle sizes was 12 nm and > 20 nm, respectively. For many catalytic applications, smaller metal particles below 2 nm are desirable, e.g.[17-18]. Shenvi et al[17] in a study of Pd clusters of different sizes, have compared the activity of the size of clusters to that of the oxidation process of CO. In their study of clusters of size ranging from Pd_n, n=1 through 25, they have found that activity to rise initially from Pd_1 to Pd_{20} followed by a decrease to Pd_{25}. In a separate study, Vadja et al[18] have found similar result. Both theoretical and experimentally, it is concluded, Pt sites of Pt_n clusters (n= 8-10), are much more active than a Pt surface for oxidative hydrogenation of propane. It has been attributed to under coordinated Pt on small Pt_n clusters. We have developed a one-step process for functionalizing nanotubes with Pt particles. Our synthesis method is simple and requires no post heat or chemical treatments. In one step, we have successfully deposited and reduced metal particles inside the tubes. Unlike other methods of metal functionalizations of tubes, the nano particles obtained are highly monodisperse, mostly < 2 nm in size and are clearly deposited along the inside walls the tubes. Also the particle dispersion on the inner walls of the tube is very uniform in comparison to other methods. This approach was successful for both supported and freestanding TiO_2 tubes. Details of tube synthesis process are described in chapter 3.

4.2 Other functionalization methods

Before going into details of photoreduction results, the metal fuctionalization results obtained in other two other techniques are described.

4.2.1 Wet method (vacuum assisted impregnation)

Mass transportation problem was one of the biggest challenges in impregnation technique. Arrays of nanotubes are closed at one end by the metal foil, trap air inside them. The trapped air suppressed insertion of metal precursor solution inside tubes. Hence in order to overcome the problem, in a modified impregnation method, liquid metal precursor was inserted inside tubes by application of vacuum. In the first step, $Cu(NO_3)_2$ solution was solidified by cooling it with dry ice. The tube sample was placed upside down on the solid $Cu(NO_3)_2$ surface. The air was then removed from the container having both $Cu(NO_3)_2$ and tube array. After 5 minutes the cooling system was removed to allow the solution to melt. After completion of melting, the tubes were let to reside inside the $Cu(NO_3)_2$ solution for further 15 minutes. Figure 4.1 presents STEM images of the nanotubes obtained in this procedure. The images show the presence of clusters of nanoparticles inside the walls of the nanotubes. This procedure showed metal particles inside tubes but it was hard to control the particle size and post heat treatment resulted in damage of tubes.

4.2.2 Gas method – CVD – *in-situ*

Arrays of self-organized TiO_2 nanotubes were synthesized by anodization of polished and cleaned Ti foils in fluoride mediated ethylene glycol solvent, using a Pt foil as cathode. *In-situ* ETEM studies for gas phase tungsten insertion were performed on as-prepared tubes in the presence of tungsten carbonyl, $W(CO)_6$) precursor as a model for our study. *In-situ* ETEM studies were performed in an FEI Tecnai F20 field emission environmental transmission electron microscope (ETEM) operating at 200kV with a point resolution of 0.24nm. TiO_2 nanotubes were heated to 300^o C in vacuum and the $W(CO)_6$ precursor

was admitted into the microscope column at a pressure of 0.01 Torr and the reaction was performed for 6 minutes.

Figure 4.2a shows the TEM image of a set of TiO_2 nanotubes before and after the exposure of $W(CO)_6$ precursor gas. From the image it can be clearly seen that the bare TiO_2 nanotubes (Figure 4.2b) were totally covered with small nanoparticles (even the holey-carbon support was covered with the nanoparticles). The average grain size of the thin film deposited on the TiO_2 nanotubes was measured to be 1.2 +/- 0.2 nm (Figure 4.3). Lattice measurement from the high resolution TEM images of these nanoparticles was measured to be 0.23 +/- 0.01 nm which matched with the W (110) d spacing. These nanoparticles were formed by the thermal decomposition of $W(CO)_6$. To determine whether the nanoparticles were deposited along the internal surface or external surface of the nanotubes, we measured the change in internal and external diameter of the tubes before and after deposition. The average internal and external diameters of the nanotubes before the deposition were 40.1 +/- 6.1 nm and 74.0 +/- 7.9 nm respectively, whereas after the deposition the average values for internal and external diameter were 32.5 +/- 5.7 nm and 84.7 +/- 9.1 nm. This shows that the internal diameter shrinks whereas the outer diameter increases after the exposure to $W(CO)_6$ suggesting that the nanoparticles were deposited on both inside and outside the nanotubes. The average internal and external deposition rates were calculated to be 30 nm/sec/Torr and 74 nm/sec/Torr respectively. After careful measurement of changes in diameter at various points it is noticed there is no significant change in the deposition rate along the tube length. This could be due the short duration and/or low temperature of the deposition allowing the gas to flow uniformly along the inside of the tube. Based on our study of nanotubes of length

up to 500 nm, we notice no mass transportation limitation on the internal deposition rate. A uniform W metal deposition in TiO_2 was obtained by using this CVD method. This method is however effective for metal functionalization, but not cost effective considering amount of precursor inside chamber.

4.3 Photoreduction of Pt

4.3.1 On anatase powder

For a typical metal functionalization experiment, 0.015 g of $PtCl_4$ was dissolved in a 15 mL of 1:1 solution of methanol and water. The solution was stirred at a low speed with magnetic stirrers to impregnate the solution and remove trapped air within the tubes. Both supported and freestanding tubes were immersed in the solution. A low pressure mercury arc lamp (USHIO) with a narrow range of wavelength and a peak value of 306 nm was used to reduce the metals (the open end of supported tubes was faced towards the light source) while stirring the solution. This wavelength is sufficient to create electron-hole pairs in the TiO_2. For a typical reaction, the intensity was 0.012 W/cm^2 at the surface of the tubes and the reaction time was 3 hours. After the reaction the surface of the tubes were cleaned with de-ionized water.

As a preliminary test photoreduction experiment was performed on anatase powder. Figure 4.4a shows the STEM images of Pt nanoparticles that are supported on anatase powder. Figure 4.4b shows the STEM image taken at slightly higher magnification. From the figure it can be seen that the Pt nanoparticles are very small and well dispersed on the anatase powder. Figure 4.4c shows the EDS spectrum taken from the Pt nanoparticle. From the spectrum it can be seen that there is no presence of Cl, which confirms the photoreduction of $PtCl_4$ Pt metal.

4.3.2 Inside tubes – one step technique

Inside supported TiO_2 nanotubes. From the figure 4.5a it can be clearly observed that fine Pt nanoparticles (bright dots) are dispersed along the inside wall of the nanotube. The bright contrast seen at the edge of the inner tube wall is caused by the STEM projection effect and confirms that the particles are indeed inside the nanotube. Energy dispersive x-ray spectroscopy (EDS) was collected from the functionalized tubes shown in Figure 4.5b. The spectra were recorded with a highly defocussed STEM probe to avoid radiation damage to the Pt phase. The EDS spectra recorded under these low-dose conditions showed no Cl peak at 2.62 keV, confirming the photoreduction of $PtCl_4$ to Pt metal had taken place under UV irradiation.

Figure 4.6 shows a Z-contrast image of Pt nanoparticle dispersion on a freestanding TiO_2 tube. The bright contrast along the edge of the inner tube wall and absence of particles on the thicker tube wall confirms the particles are present inside the tube. The Pt particle size distribution was measured for each type of tube from 200 particles and is shown as inset to Figures 4.5a and 4.6. The mean sizes were 1.8 ± 0.3 nm and 1.8 ± 0.4 nm for supported and unsupported tubes respectively. This is a factor of 5 times smaller compared to impregnation methods[14]. In both cases, the size distribution is rather narrow with a standard deviation of 0.4 nm or less showing that there is a very tight control over the particle size.

The freestanding tubes are up to 12 μm in length and mass transport limitations and light attenuation may cause the metal loading to drop with distance from the tube opening adjacent to the light source. To investigate this issue, we imaged the uniformity of the metal dispersion along the length of the tubes. Figure 4.7a shows a low magnification

STEM image of a 1.6 μm section of a freestanding nanotube. Figure 4.7b, 4.7c and 4.7d are images taken at higher magnification from the top, middle and bottom of the nanotube, respectively. These images clearly show the uniformity of Pt nanoparticle distribution inside a nanotube. This suggests that particle deposition is uniform along at least the first 1.6 μm length of the tube. STEM images reveal that some sections of the tube showed a much lighter metal loading (see Figure 4.8). However, it was not possible to know the original location of the section relative to the tube opening because the tubes are broken during STEM sample preparation. Note that this tube is free standing and much longer than supported tube as mentioned above. Presumable the lightly loaded section came from a location substantially greater than 2 μm below the tube opening.

Mass transport limitations could be more significant on the supported tubes because they are open only on one end. The STEM image (figure 4.9) shows the Pt nanoparticle distribution towards the closed end of a supported TiO_2 nanotube. The image clearly shows the Pt nanoparticles at the bottom of the tube. Since these tubes are 2 μm in length, this demonstrates that mass transport and light penetration are not limiting factors. It also shows that the closed end does not prevent Pt precursor solution from reaching the bottom of the nanotubes. It has been observed experimentally that methanol significantly wets the surface of the TiO_2 nanotube film compared to water. Hence the mixture of methanol and water facilitates the wetting of the surface of TiO_2 and helps the solution reach the end of the tubes.

4.3.3 Reaction Mechanism

There are two different mechanisms for reduction of $PtCl_4$ for the experimental conditions employed here. In the first mechanism, TiO_2 generates an electron-hole pair upon excitation with the light source. Methanol is a hole scavenger[19] and thus suppresses electron-hole pair recombination allowing the photo-generated electrons from TiO_2 to reduce the $PtCl_4$ that is adsorbed onto the surface. (In an electron paramagnetic resonance study Micic et al found a $^{\cdot}CH_2OH$ radical which was created by the photoinduced hole transfer from TiO_2 to chemisorbed methanol of TiO_2 surface[20]). In a second mechanism proposed by Nakamatsu et al[21], it was shown that the oxidation potential of methanol is -0.74V whereas electron at conduction band edge of TiO_2 is at -0.18V. Hence Pt reduction can occur via direct interaction with methanol.

We also conducted reduction experiments both with and without the use of TiO_2. Reduction of the solution was observed to occur in the absence of titania but the reaction rate was increased by between a factor of 2 - 4 when titania was present. This suggests a synergistic effect with both processes playing an active role in photoreduction of Pt metal in solution. However, particles formed directly in solution are likely to agglomerate into larger particles. Thus the small particles on the oxide surface are most likely formed by the first mechanism involving both the titania and methanol.

4.4 Summary

A one step photoreduction technique has been developed to generate a fine dispersion of Pt particles inside supported and free standing TiO_2 nanotubes arrays. Z-contrast STEM showed that the average Pt particles were less than 2 nm in size and the particles were

uniformly dispersed to a depth of at least 1.6 mm in the free standing tubes. For the supported TiO_2 tubes, particles were uniformly disperse to the closed end 2 mm below the tube opening showing that mass transportation limitations were not a significant problem. UV light attenuation resulted in a lighter metal loading at a depth below 2 mm. For supported TiO_2 nanotubes, the photoreduction approach is attractive because metal should only be deposited along the tube to a depth comparable with the photon penetration depth. Moreover, the metal particles will nucleate at active points on the titania surface where photoelectrons reach the surface. The metal functionalization process is simple and involves only one step and no post heat treatment.

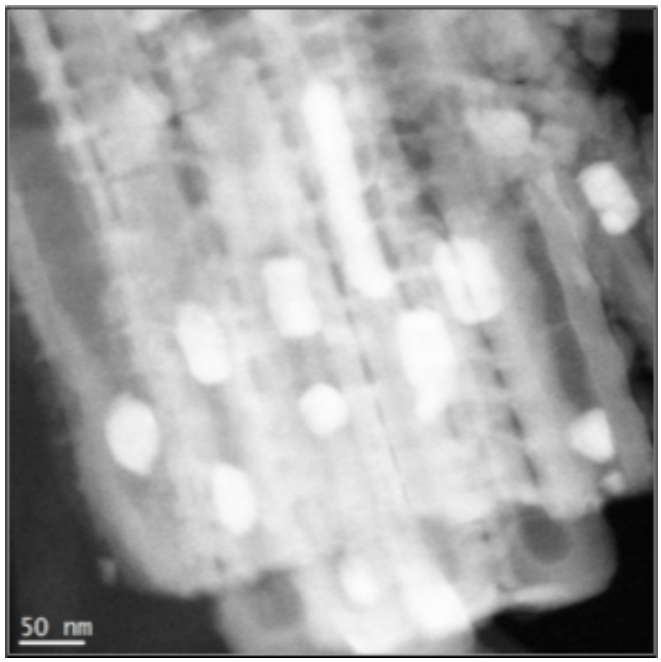

FIG. 4.1. STEM image showing much lighter loading of Pt nanoparticles inside the tube, which could be due to the UV light attenuation effect in a tube after a length of 2 mm.

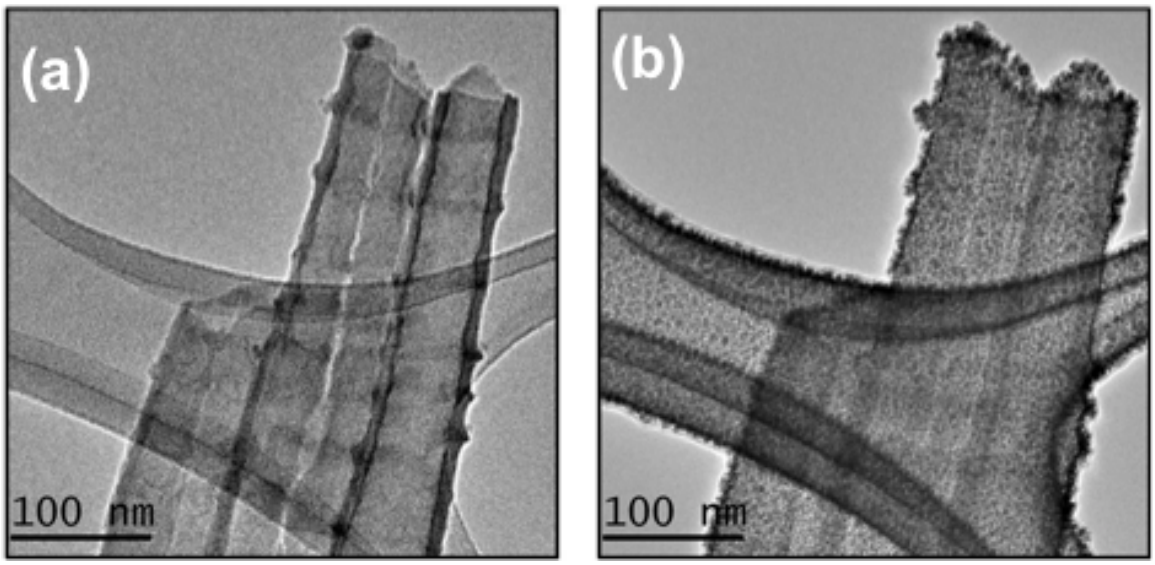

FIG.4.2a and b. *In-situ* environmental TEM images of TiO_2 nanotubes at 300^{o}C a) before deposition b) after $W(CO)_6$ deposition .

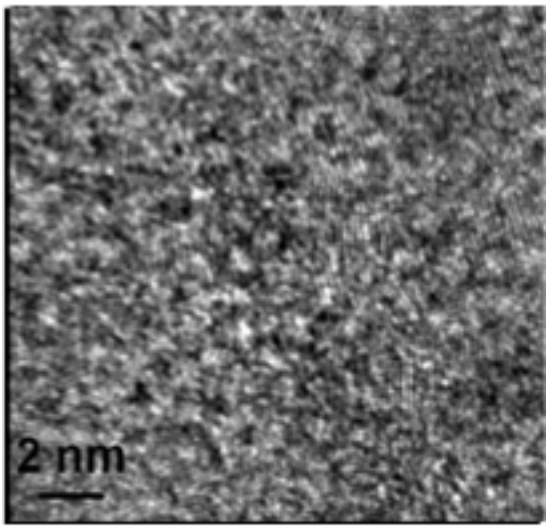

FIG. 4.3. HREM image of W particles showing grain size distribution.

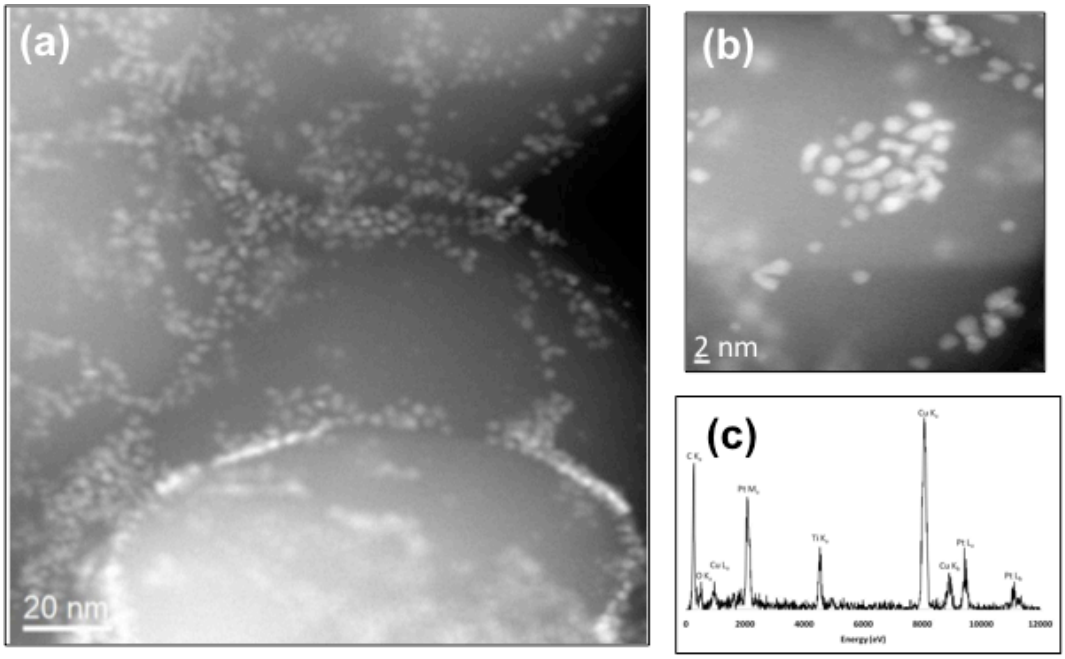

FIG. 4.4. STEM image of Pt nanoparticles on anatase particles, (b) is a high magnification image of the same (c) EDS acquired from the nano particles proving it is Pt.

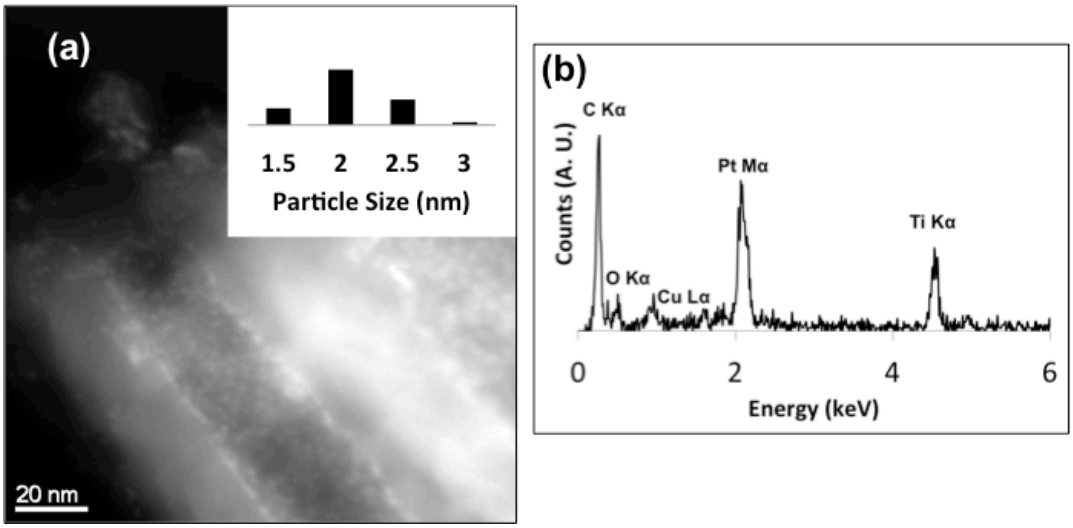

FIG.4.5. STEM image showing the Pt nanoparticle dispersion in the supported TiO_2 nanotubes that were open on one end and closed on the other end. b) EDS collected from particles. Inset is the particle size distribution inside tube.

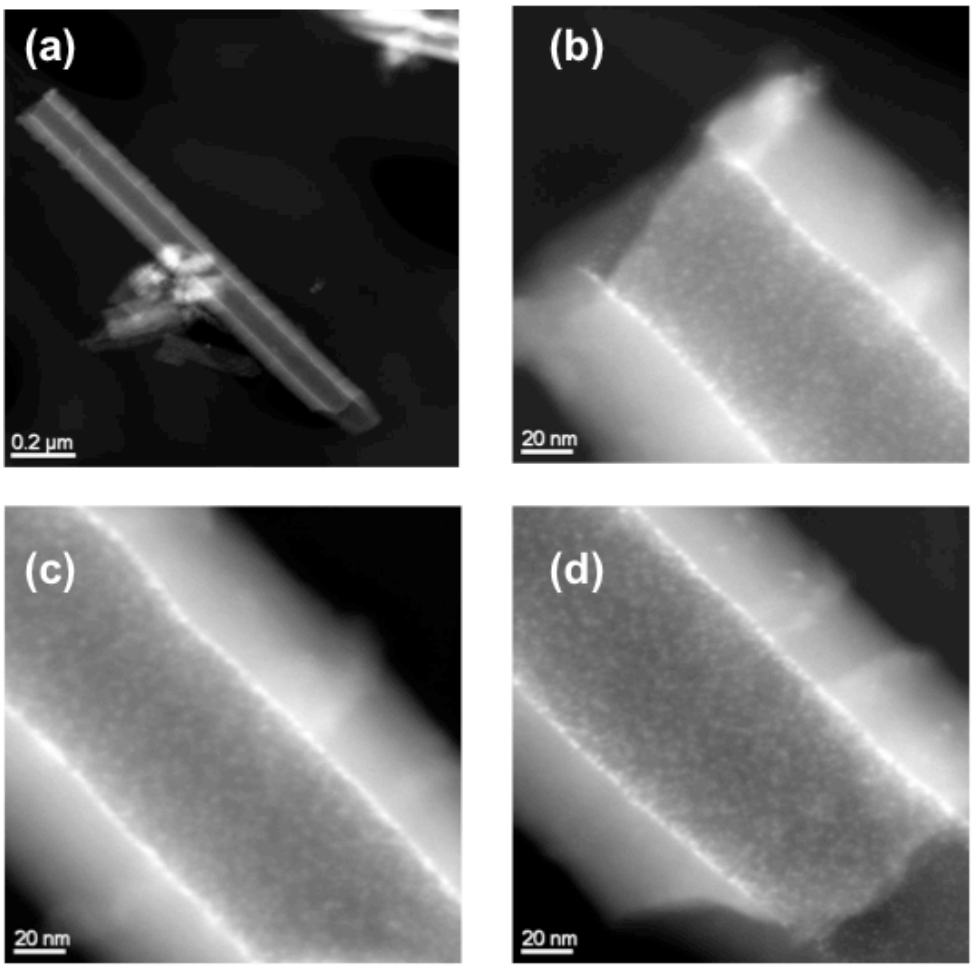

FIG. 4.6. STEM image showing the Pt nanoparticle dispersion in freestanding TiO_2 nanotubes that is open at both ends. Inset is the particle size distribution inside tube.

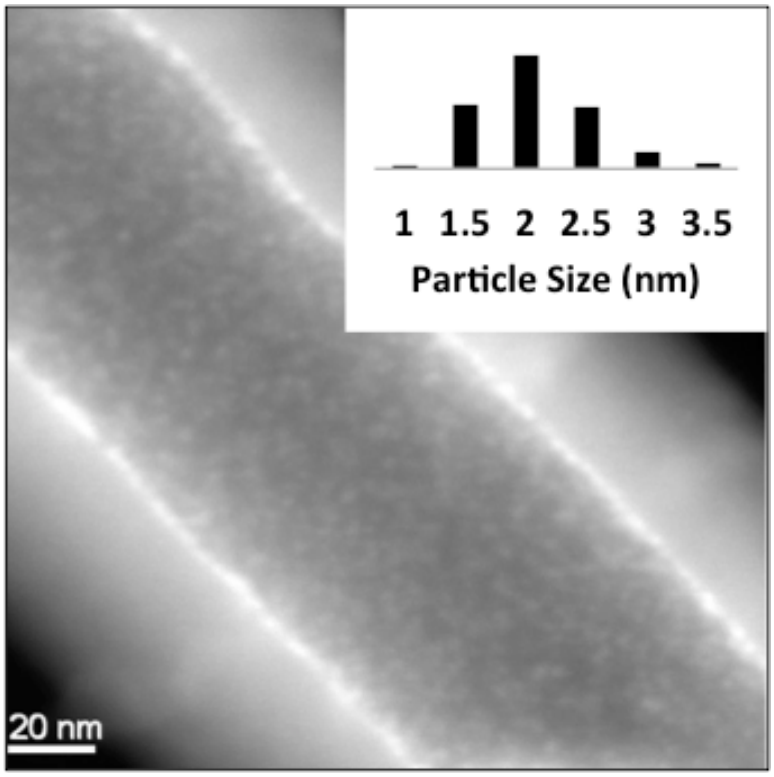

FIG. 4.7. STEM images showing the Pt nanoparticle distribution on TiO_2 nanotubes that were open on both ends. a) low magnification image showing the full length nanotube, b), c) and d) are the blow up images from top, middle and bottom of the nanotube respectively showing the presence of Pt nanoparticles.

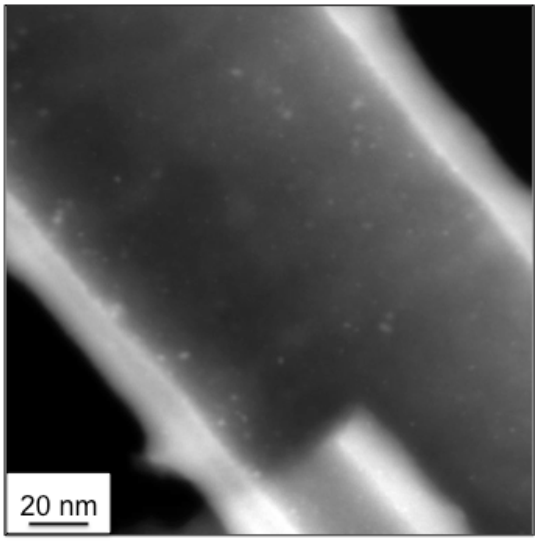

FIG. 4.8. Lighter loading of Pt in free standing tube

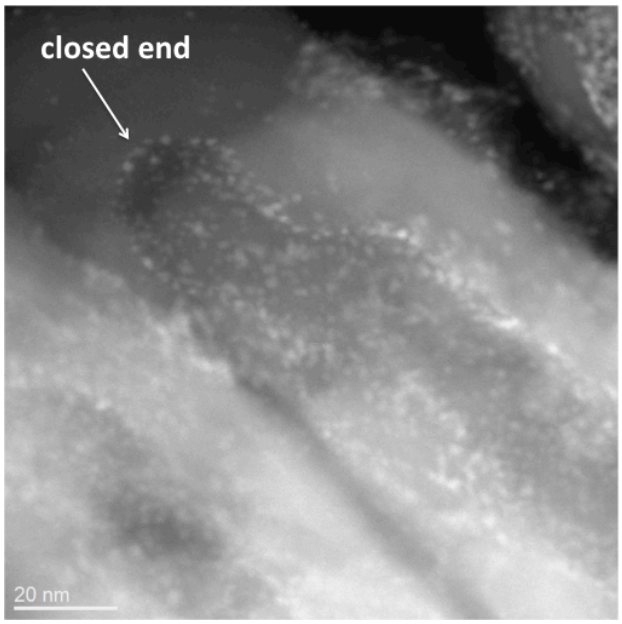

FIG. 4.9. STEM image showing the Pt nanoparticle distribution towards the closed end of the TiO_2 nanotubes that were closed on one end.

Reference

1. T. Akita, M. Okumura, K. Tanaka, S. Tsubota, Structural analyses by TEM of iridium deposited on TiO2 powder and rutile single crystal. *J. Electron Microsc.* **53,** 29 (2004)

2. S. Tsubota, T. Nakamura, K. Tanaka, M. Haruta: Effect of calcination temperature on the catalytic activity of Au colloids mechanically mixed with TiO_2 powder for CO oxidation. *Catal. Lett.* **56**, 131 (1998)

3. S.A.C. Carabineiro, B. F. Machado, G. Drazic, R.R. Bacsa, P. Serp, J.L. Figueiredo, and J.L. Faria: Photodeposition of Au and Pt on ZnO and TiO_2. *10^{th} International Symposium Scientific Bases for the Preparation of Heterogeneous Catalysis* **175**, 629 (2010)

4. K. Maeda, M. Higashi, D. Lu, R. Abe, and K. Domen: Efficient Nonsacrificial Water Splitting through Two-Step Photoexcitation by Visible Light using a Modified Oxynitride as a Hydrogen Evolution Photocatalyst. *J. Am. Chem. Soc.* **132**, 5858 (2010)

5. J. Ohyama, K. Teramura, S-i Okuoka, S Yamazoe, K. Kato, T. Shishido, and T. Tanaka: Investigation of the Formation Process of Photodeposited Rh Nanoparticles on TiO_2 by In Situ Time-Resolved Energy-Dispersive XAFS Analysis. *Langmuir*. **26**, 13907 (2010)

6. J. Ohyama, A. Yamamoto, K. Teramura, T. Shishido, and T. Tanaka: Modification of Metal Nanoparticles with TiO_2 and Metal−Support Interaction in Photodeposition. *ACS Catal.* **1**, 187 (2011)

7. T. Sano, N. Negishi, K. Uchino, J. Tanaka, S. Matsuzawa, K. Takeuchi: Photocatalytic degradation of gaseous acetaldehyde on TiO_2 with photodeposited metals and metal oxides. *J. Photochem. Photobiol. A*. **160**, 93 (2003)

8. J. Taing, M. H. Cheng, and J. C. Hemminger: Photodeposition of Ag or Pt onto TiO_2 Nanoparticles Decorated on Step Edges of HOPG. *ACS Nano.* **5**, 6325 (2011)

9. M. Berr, A. Vaneski, A. S. Susha, J. Rodríguez-Fernández, M. Döblinger, F. Jäckel, A. L. Rogach, and J. Feldmann: Colloidal CdS nanorods decorated with subnanometer sized Pt clusters for photocatalytic hydrogen generation. *Appl. Phys. Lett*. **97**, 093108-1 (2010)

10. C. Pacholski, A. Kornowski, and H. Weller: Site-Specific Photodeposition of Silver on ZnO Nanorods. *Angew. Chem. Int. Ed*. **43**, 4774 (2004)

11. J. Liu and F. Chen: Plasmon Enhanced Photoelectrochemical Activity of Ag-Cu Nanoparticles on TiO2 /Ti Substrates. *Int. J. Electrochem. Sci*. **7**, 9560 (2012)

12. Y. Qu, T. Xue, X. Zhong, Y.-C. Lin, L. Liao, J. Choi, and X. Duan: Heterointegration of Pt/Si/Ag Nanowire Photodiodes and Their Photocatalytic Properties. *Adv. Funct. Mater.* ***20***, 3005 (2010)

13. G. Dukovic, M. G. Merkle, J. H. Nelson, S. M. Hughes, A. P. Alivisatos: Photodeposition of Pt on Colloidal CdS and CdSe/CdS Semiconductor Nanostructures. *Adv. Mater.* **20**, 4306 (2008)

14. M. Tian, G. Wu, A. Chen: Unique Electrochemical Catalytic Behavior of Pt Nanoparticles Deposited on TiO2 Nanotubes. ACS *Catal*. **2**, 425 (2012)

15. H. Bian, Y. Wang, B. Yuan, J. Cui, X. Shu, Y. Wu, X. Zhang, and Adeloju: Flow-through TiO_2 nanotube arrays: a modified support with homogeneous distribution of Ag

nanoparticles and their photocatalytic activities. *New J. Chem*. **37**, 752 (2012)

16. K. Chen, X. Feng, R. Hu, Y. Li, K. Xie, Y. Li, H. Gu: Effect of Ag nanoparticle size on the photoelectrochemical properties of Ag decorated TiO_2 nanotube arrays. *J. Alloy Compd.*, **554**, 72 (2013)

17. W.E. Kaden, T.Wu, W.A. Kunkel, S.L. Anderson: Electronic Structure Controls Reactivity of Size-Selected Pd Clusters Adsorbed on TiO_2 Surfaces. *Science.* **326**, 826 (2009)

18. S. Vajda, M. J. Pellin, J. P. Greeley, C. L. Marshall1, L. A. Curtiss, G. A. Ballentine, J. W. Elam, S. Catillon-Mucherie, P. C. Redfern, F. Mehmood , P. Zapol: Subnanometre platinum clusters as highly active and selective catalysts for the oxidative dehydrogenation of propane. *Nature Mats.* **8**, 213 (2009).

19. V. Iliev, D. Tomova, L. Bilyarska, A. Eliyas, L. Petrov: Photocatalytic properties of TiO_2 modified with platinum and silver nanoparticles in the degradation of oxalic acid in aqueous solution. *Appl. Catal., B.* **63**, 266 (2006)

20. O. I. Micic, Y. Zhang, K. R. Cromack, A. D. Trifunac, M. C. Thurnauer: Photoinduced hole transfer from titanium dioxide to methanol molecules in aqueous solution studied by electron paramagnetic resonance. *J. Phys. Chem.* **97,** 13284 (1993)

21. H. Nakamatsu, T. Kawai, A. Koreeda, S. Kawai: Electron-microscopic Observation of Photodeposited Pt on TiO_2, Particles in Relation to Photocatalytic Activity. *J. Chem. Soc., Faraday Trans. 1* **82**, 527 (1986)

CHAPTER 5

SUMMARY AND FUTURE WORK

5.1 Summary

The work presented in this thesis is composed of two parts. In one part phase and morphology of titania tubes has been investigated in different temperature environments. This is discussed in detail in third chapter. In the second part, the titania tubes are functionalized with different metals via photoreduction technique. The photoreduction technique is further utilized to make bimetallic systems of Ag and Pt on anatase powder. The photoreduction results are discussed in chapter 4 and partly in appendix.

5.2 Phase and morphology study of TiO_2 nanotubes

TiO_2 nanotubes were prepared via anodization. The as-prepared tubes were annealed at several temperatures in order to obtain different combinations of phases. The resulting phases along with the effect of heat treatment and thus the morphology of the tubes were investigated. XRD was used to determine the bulk phase of the tubes whereas in TEM was employed to determine the nanostructure. Heating amorphous tubes transformed the tubes to anatase; with further heating they start transforming to rutile at approximately 500 ^{o}C, at higher temperature of 800 ^{o}C, the tubes are completely transformed to rutile. *In-situ* results were compared with *ex-situ*; it was found that unsupported tubes do not convert to rutile even at 800 ^{o}C. The metal-oxide interface is the source of this conversion. This interface facilitates oxygen vacancies and hence the conversion.

5.3 Metal functionalization of the tubes

Pt nano particles were photo reduced inside titania nanotubes using a photo reduction technique. The particles were 2 nm on average in size. In a similar procedure Ag particles were deposited, with average particle size of 10 nm. In both cases the size distribution was monodisperse. Light induced electron-hole pairs available from titania as well as methanol as a reducing solvent both act as synergistic factors in the reduction process.

In bimetallic photo deposition of Ag and Pt , Pt was deposited followed by Ag. Ag was found to be enhancing the reduction process of Pt on the titania surface. EDS results confirmed the presence of both metals in clusters. At various reactions times, Pt was found to be deposited, initially onto Ag, gradually increasing in amount, and finally depositing onto the surface of titania independently.

5.4 Future Work

There are several possibilities of future expansion of the current work presented in the thesis.

(i) Qualitative and semi quantitative EDS study was done on bimetallic systems. Detailed quantitative analysis can be done using Cliff-Lorrimor equation, after collecting EDS data from several clusters.

(ii) Similarly, other reducible metals can be used to deposit with Ag to make bimetallic systems.

(iii) Preliminary work on *in-situ* photoreduction study of Pt onto anatase has been done (appendix). More studies have to be performed in order to find molecular level

mechanism of photo reduction process while performing the reaction in environmental microscope in presence of light source.

(iv) After initial study of catalytic performance, most optimized tubes can be prepared to enhance the photocatalytic efficiency of tubes.

APPENDIX

I. CO_2 reduction with H_2 gas

The catalytic properties of TiO_2 tubes were estimated in CO_2 reduction with H_2 gas. The resulted gas, methane, was detected and estimated in a Varian GC, FID detector. The tubes, as prepared, and annealed at various temperatures were compared with that of with commercial P-25 and copper deposited P-25. The result is summarized in table I as below.

Table I CO_2 reduction efficiency with TiO_2 in volume of methane production.

Catalyst	Phase	Source UV (μ, nm)	Methane (ppm)
Tube, as prepared		254	20.21
Tube, annealed at 450 ^oC	Mostly anatse	254	41
Tube, annealed at 600 ^oC	Anatase + rutile	254	20
P-25	Anatase + rutile	306	1.65
P-25, 5% Cu	Anatase + rutile	306	13.6

II. Other synthesis results to functionalize TiO_2 tubes

A three-electrode system was employed for the electrochemical deposition: the working and counter electrode served as TiO_2 nanotube and Pt foil respectively. $PtCl_4$ was used as

the electrolyte. The voltage and time of deposition are carefully adjusted and optimized for the growth and insertion of the particle. With an increase in voltage large particles were observed as shown in the SEM image in figure II below.

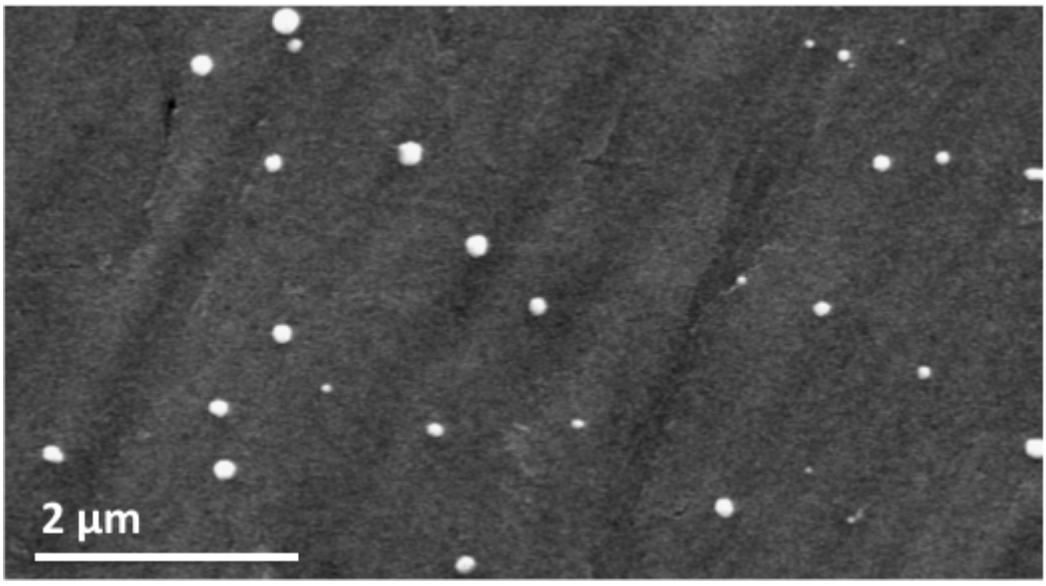

FIG. II. Pt nano particles deposited on surface of TiO_2 arrays of tubes.

III. Metal particle stuffed nanotube

The photo reduction of Pt into the tube, described in chapter 4 was done on a freshly prepared tube pre-immersed in alcohol solution in order to avoid any air trapped at any moment. This resulted in TiO_2 tubes heavily stuffed with fine Pt nanoparticles as shown in image below.

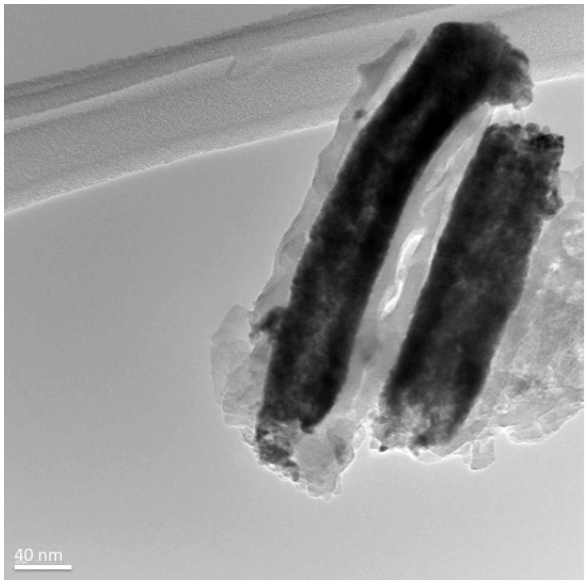

FIG. III. Metal nano particles filling up tubes.

IV. Secondary ion mass spectroscopy (SIMS) data

SIMS was used to quantify the metals present in both Pt and Ag functionalized tubes. A probe of 1 micron was used to collect signal from 50-100 nm deep areas of both samples. Pt and Ag in tubes were found to be 12 and 5.85 atomic percent respectively.

V. Catalytic data – Methylene blue dye degradation

Methylene blue dye degradation was used as a model test to measure and compare the photocatalytic efficiency of TiO_2 tubes, bare, annealed at various temperatures and functionalized with different metals. Methylene blue (MB) is an organic dye that has an intense blue color. It gives a characteristic absorption spectrum. MB degrades upon exposure to light over time up to a certain extent. However, in presence of a catalyst, the degradation is modified. Hence, the phenomena can act as a measure for catalytic efficiency of a catalyst.

In a typical set up, MB solution of $1x10^{-5}$ M concentration was obtained in a covered petri dish with catalyst placed on a magnetic stirrer. The UV light source was provided on the top of the solution. For a long time period, the measurement was not done and UV light was not exposed to the solution. At this phase the catalyst was allowed to decrease the dye intensity without any an absolute dark condition. The drop in dye intensity was measured time to time in UV-VIS spectrophotometer. After the dye intensity (absorbance value obtained) attain a constant value, the light source for the photocatalytic experiment was illuminated over the solution. The drop in dye intensity was further observed due to presence of catalyst and thus measured up to 2.5 hrs. The plots (figure V1 and V2) below are the results of tubes, annealed at various temperatures and that of metal functionalized.

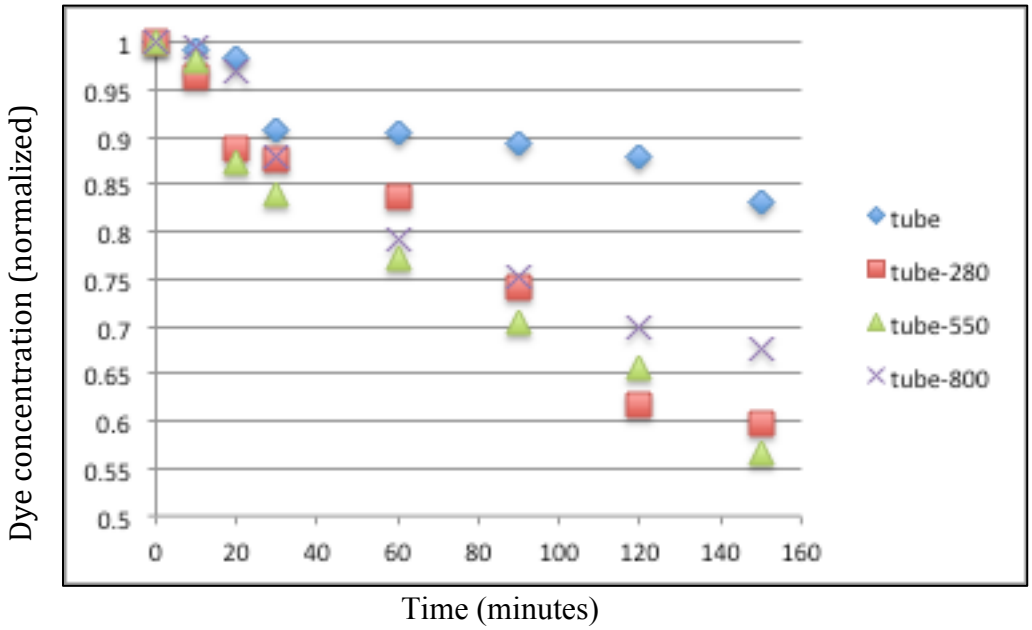

FIG V1. Dye concentration drop with time on tubes annealed at different temperature, tubes annealed at 280 ^{o}C, 550 ^{o}C and 800 ^{o}C are denoted as tube-280, tube-550 and tube-800 respectively.

Tubes annealed at, 800 ^{o}C, perform as well as others, however after around 80 minutes the performance decreases. Overall, tubes annealed at 550 ^{o}C shows best catalytic performance.

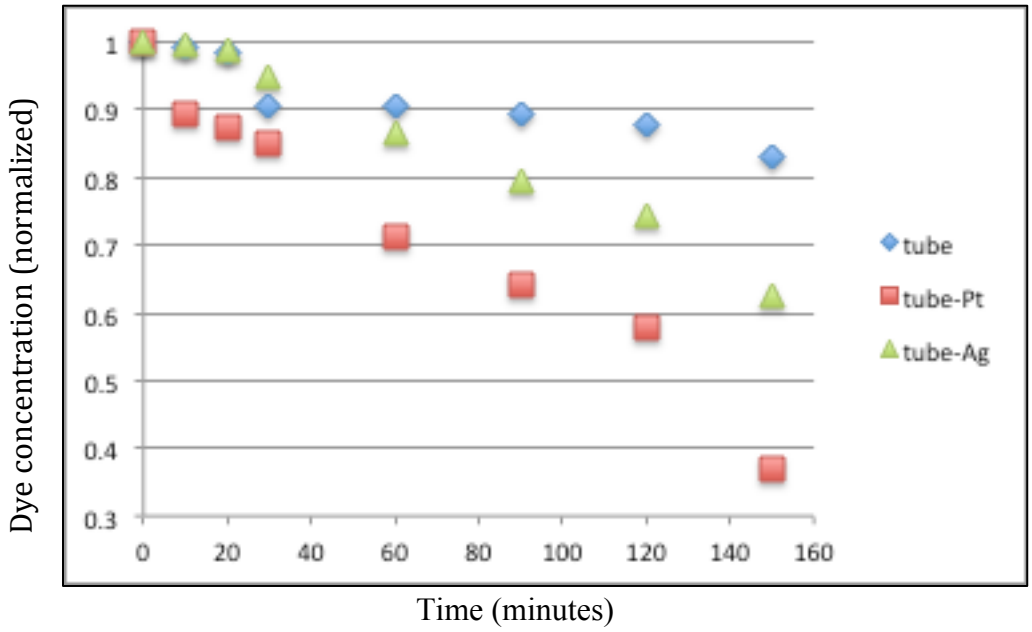

FIG V2. Dye concentration drop with time on different metal functionalized tubes

The concentration of dye is decreased by more than 60% after 150 min by Pt functionalized tubes and by 40% by Ag functionalized tubes. However it is not safe to compare the two cases, since the particle sizes are different and the amount of metals in each also vary.

VI. Preliminary data of *in-situ* photoreduction of Pt on anatase

For a photoreduction of Pt on anatase study in *in-situ* technique, as the chemical reaction described in chapter 4, a mixture of alcohol and water has to be used as solvent just as in *ex-situ* condition for the experiment. The solvent has to be inserted into reaction chamber

via a pumping system by evaporating the mixture of gases followed by condensing onto the cold stage bearing the sample on it. In order for a mixture of two liquids to evaporate and again condense with same composition, they have to form an azeotropic mixture. Methanol does not form azeotropic mixture with water at any composition but ethanol forms such mixture with water at 95.5 wt% of ethanol solution in water. An *ex-situ* reaction was performed with this mixture on anatase powder with $PtCl_4$ as precursor under similar experimental condition as described in chapter 4. The photoreduced anatase powder was observed in TEM. Figure below shows the photoreduced Pt metal particles on anatase powder. A similar reaction mixture can be used for *in-situ* reactions.

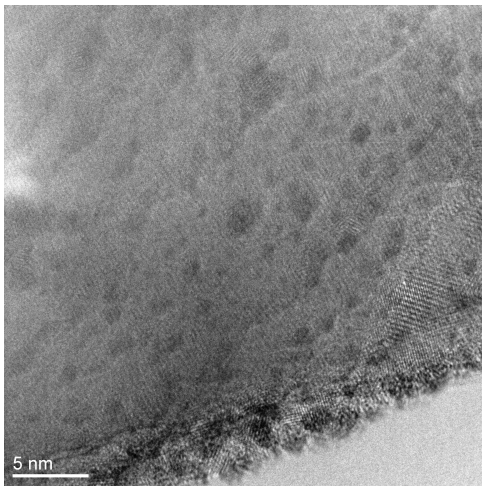

FIG VI. Pt deposited on anatase powder using ethyl alcohol solution

VII. AgPt bimetallic results

Ag on anatase powder – achieving well dispersed Ag on anatase and in tubes:

Ag was deposited onto anatase powder using similar technique as Pt as described in the previous chapter. $AgNO_3$ being an extremely photosensitive material, the reduction process was very fast typically occurring on the second timescale. Hence very small Ag nano particles with a homogeneous distribution was obtained in 16 seconds with fixed 9.7m mW/cm^2 UV light intensity. Figure VII-1 shows a typical size distribution (~ 1-2 nm) of Ag particles on anatase powder. However, since the reaction time was very small, attaining small particles inside the tube and at the same time achieving uniformity in distribution was hard under similar reaction condition. Figure VII-2a shows Ag particles in tubes. In presence of UV light, where the reaction was fast, huge particles were seen agglomerating on the mouth of tubes, which were closer to the light source, with fewer Ag particles found inside the tube. In a second experiment, laboratory lights instead of UV lights were used for the reaction with the TiO_2 tubes. Tubes were merged in a Ag solution for 4 hrs and left on the laboratory bench. These tubes were investigated and found to have uniform Ag particles. Figure 2b presents uniform Ag particles of average ~ 10 nm. Inset is the size distribution of Ag inside tube.

Phase analysis:

The as prepared Ag on anatase powder was analyzed in XRD for phase identification. Figure VII-3 shows an XRD pattern obtained which has solid lines indicating anatase reflections and the dotted lines are marked to be (200), (220) and (311) planes of cubic Ag metal. However the experimental two-theta values of the above planes found to be 44.6, 64.8 and 77.8 against 44.27, 64.42 and 77.47 respectively in bulk Ag

metal. Hence, there is a systematic 0.4 two-theta increase, which confirms a decrease in d values of Ag nano particles. The reason could be attributed to the very small size of nanoparticles, in which bond lengths shrinks to accommodate dangling bonds on surface to minimize surface energy.

Stability of Ag nano particles in other metal solutions:

In the bimetallic systems in this study, Ag was used as host metal while another metal was targeted to be the guest metal in the systems. In order to make bimetallic systems, the stability of the second metal in the presence of Ag deposited anatase powder was studied. The sample of anatase powder as shown in figure 1 was used. A second metal precursor solution of M (M= Cu, Ni, Pt) was mixed with Ag deposited anatase powder without any UV light exposure in dark condition with mild stirring. The result was monitored after 10 and 20 minutes of stirring. While the results show that after 10 minutes there is no Ag particles left on anatase powder in Pt solution (Figure VII-4a), after 20 minutes there is still some Ag present in Cu and Ni solution (Figure VII-4b and c). The result can be attributed to the reduction potential argument of Ag with respect to other metals. The reduction potential of Pt (+ 1.14 V) is higher than that of Ag (+ 0.79 V), thereby dissolve Ag ions. However, Cu (+ 0.34 V) and Ni (- 0.26 V) have reduction potentials lower than that of Ag. Based on the above observations, it was understood that Ag particles as small as 1-2 nm are very unstable in other metal solutions, especially with Pt metal solution. Hence bigger Ag particles were sought in synthesis.

Bigger Ag nano particles synthesis using photoreduction technique (plasmonic effect of Ag)

In order to increase the particle size of Ag obtained so far, combinations of higher light intensity and longer reaction times (more than 16 sec) were employed. In various attempts to increase the size, it was noticed (figure VII-5a through c) that bigger Ag particles were occasionally found while most of the particles are still very small as in figure 1, i.e. 1-2 nm in size. As the reaction proceeded beyond 16 sec, the color of the solution became more dark, which suggested an increase in Ag particle size and/or more Ag metal particle production in solution and/or anatase surface. However, the result did not show a visible increase in existing Ag particles size nor particles density on the anatase surface, hence leaving the only possibility of more Ag particle formation in the solution. Hence the strategy of 2-step photoreduction was employed. In a two step process, the original excess Ag precursor solution was discarded after 16 seconds of reaction to collect the Ag deposited anatase powder. In the second step, fresh Ag solution was used to continue identical 1st step. Hence the existing Ag metals can act as host sites of the new Ag metals to be deposited. Figure VII-6a and b show the improved result obtained via such two-step technique. It has more Ag particles of 2-5 nm size, with few > 5 nm present.

Bimetallic results – AgPt

AgPt bimetallic system was synthesized via photoreducing Ag metal followed by Pt onto anatase powder. In a first step Ag was deposited on anatase powder. Pt was deposited using photoreduction procedure onto Ag deposited anatase. Results of three

different duration of reaction times of Pt deposition were compared. After 10, 35 and 45 minutes of Pt photo deposition onto Ag deposited anatase, the sample was collected and investigated to see the nature of metals deposition. Figure VII-7a has 10 minute of Pt reduction reaction with a EDS (figure VII-7b) collected from a clustered area. The EDS result confirms presence of both metals. After 35 minutes of reactions (in figure VII-8) EDS were collected from various areas. Similar collection was done from sample from reaction time of 45 minutes (shown in figure VII-9). Comparing the results at both few interesting results are observed.

(i) Almost all clusters have both metals present – This shows the method was successful in giving a bimetallic system.

(ii) Pt is not found independent at any cluster (without Ag) at 35 minutes – This suggests up to 35 minutes of reduction times, Pt was deposited preferentially at Ag sites.

(iii) At 45 minutes, relative more amount of Pt is found in clusters – suggesting more deposition of Pt on to the Ag in comparison to 35 minutes.

(iv) No cluster is found to be only of Ag after 45 minutes – all Ag sites are codeposited with Pt.

(v) Independent Pt cluster is found – suggests between 35-45 minutes of reaction time, all Ag sites are saturated with Pt, hence prompting to formation of newer Pt independent sites.

The above observations revealed that Ag is acting as a site facilitating the reduction of Pt. The fact that there is no independent Pt site found initially, reveals that up to this 35-45 min time period, Pt got deposited only onto Ag sites. After this time, the saturation Pt at Ag sites occurred and independent Pt clusters are nucleated.

This further suggests that TiO_2 anatase surface acts as reduction site (by providing electron available generated from electron-hole pair)

A qualitative and semi quantitative analysis of EDS collected and presented in figures 7 through 9 shows how metals depositions have varied from 10 through 45 minutes. During 10 minutes of reaction, it is noticed relatively more amount of Ag is present in the clusters. In figure 8, EDS was collected from four different areas. In bigger spots, relatively more Pt is found, where as in smaller ones are seen with lesser Pt. The variation of contrast presents distribution of two metals in a cluster. After 45 minutes of reaction, EDS results shows even more amount of Pt in the clusters than the previous times. In Figure VII-10, marked, as spot 4 is an example of individual Pt formation after 45 minutes of reaction.

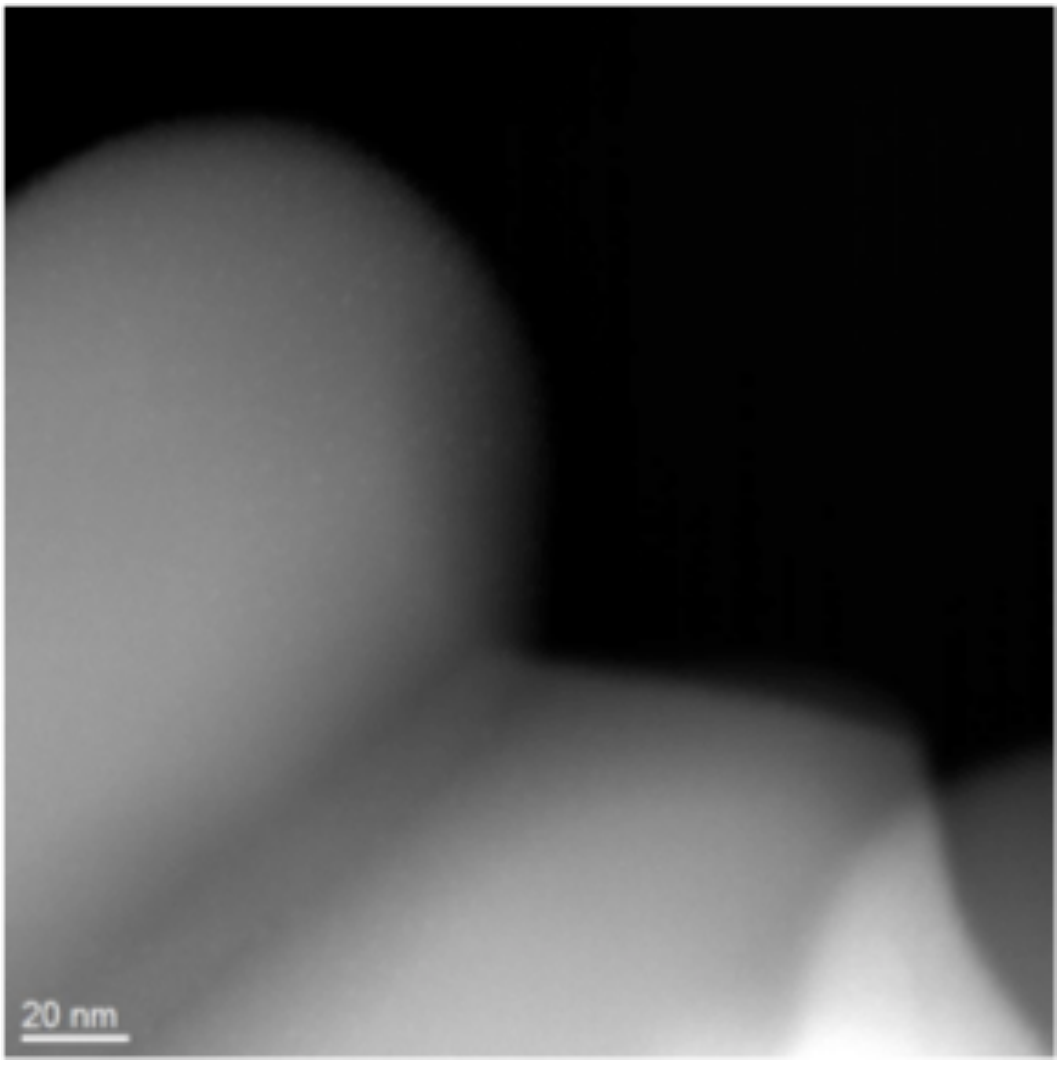

FIG. VII-1. STEM image showing Ag nanoparticles on anatase

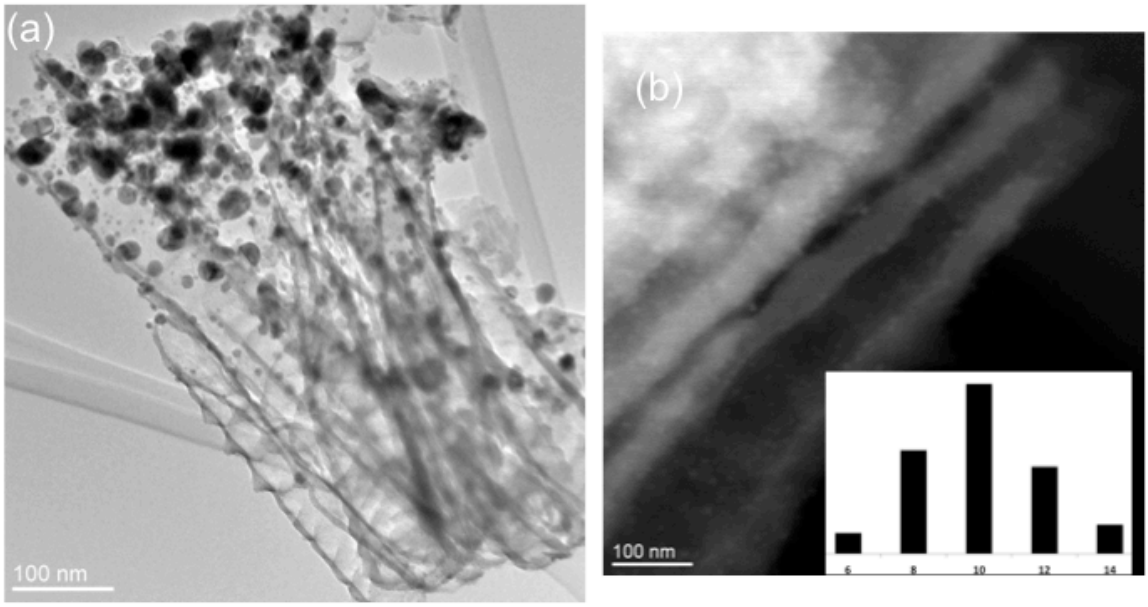

FIG. VII-2. STEM image (a) showing bigger Ag nano particle at the mouth of the tube, while very less particles inside (b) controlled synthesis where uniform small Ag particles are inside tubes

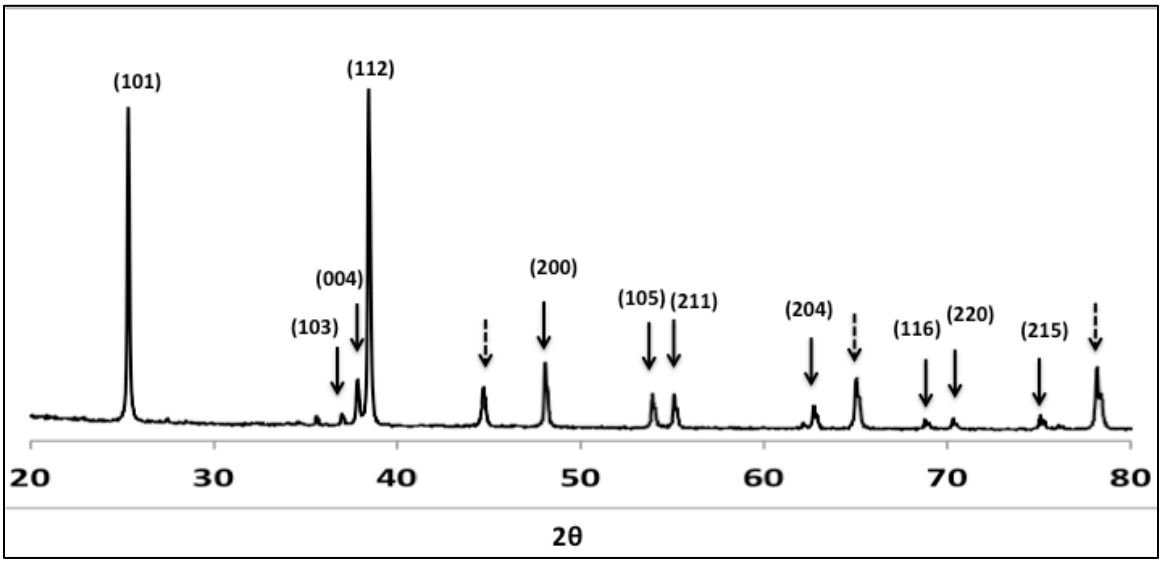

FIG. VII-3. XRD of Ag on anatase sample, solid line stands for anatase and broken lines correspond to cubic Ag.

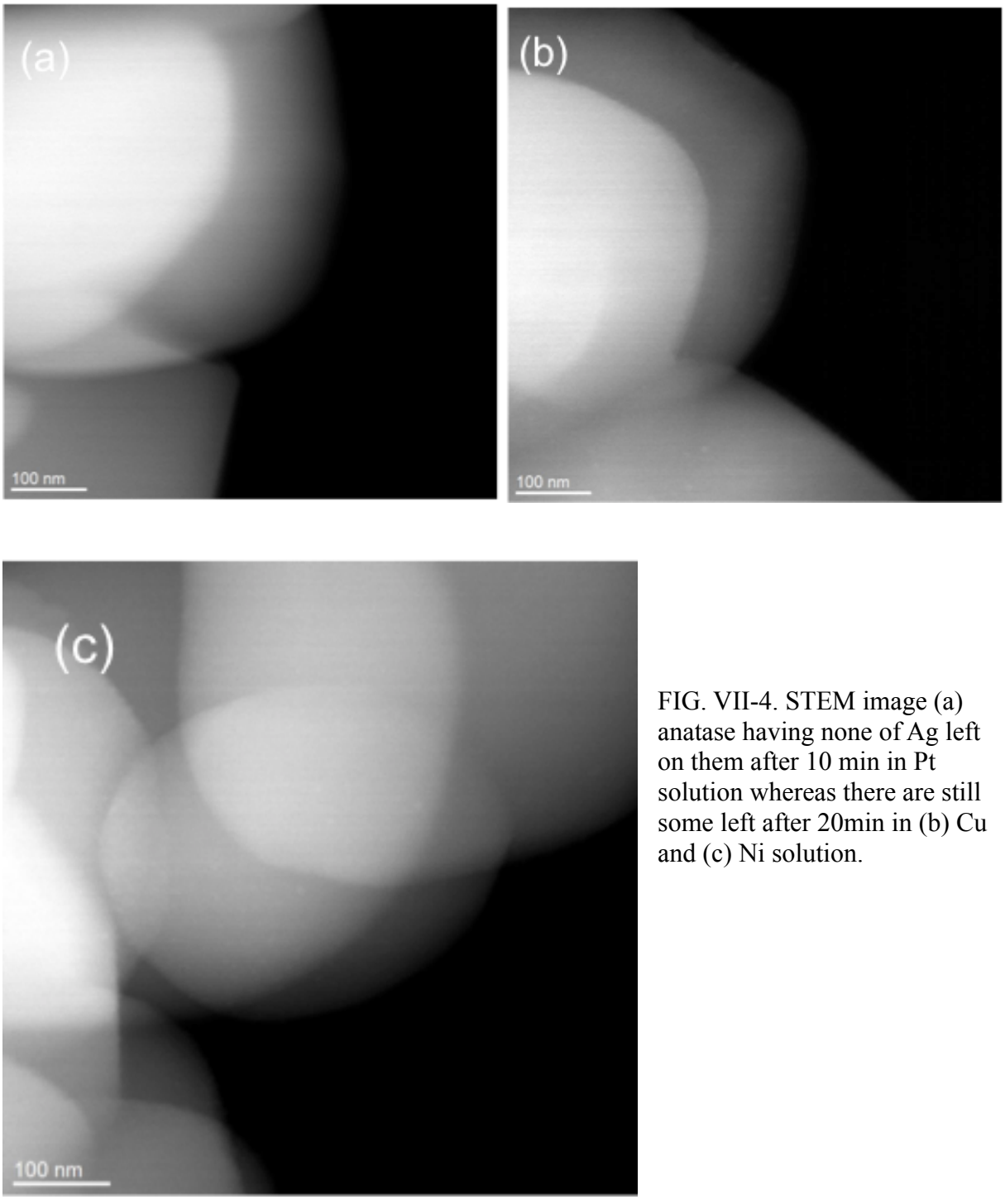

FIG. VII-4. STEM image (a) anatase having none of Ag left on them after 10 min in Pt solution whereas there are still some left after 20min in (b) Cu and (c) Ni solution.

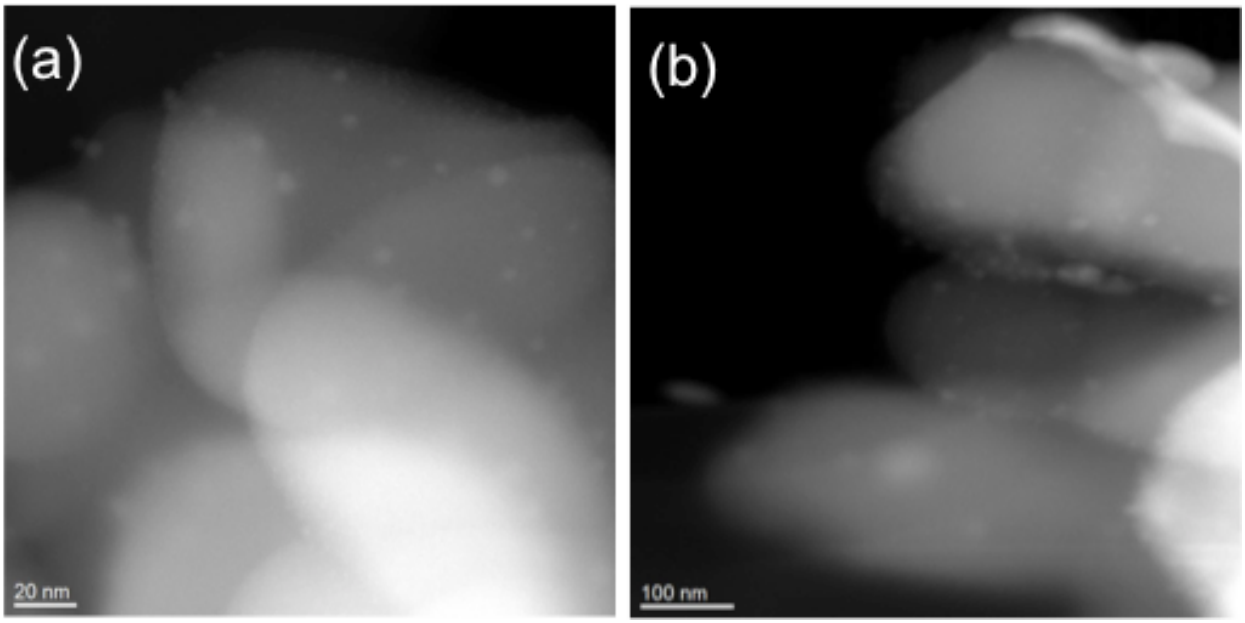

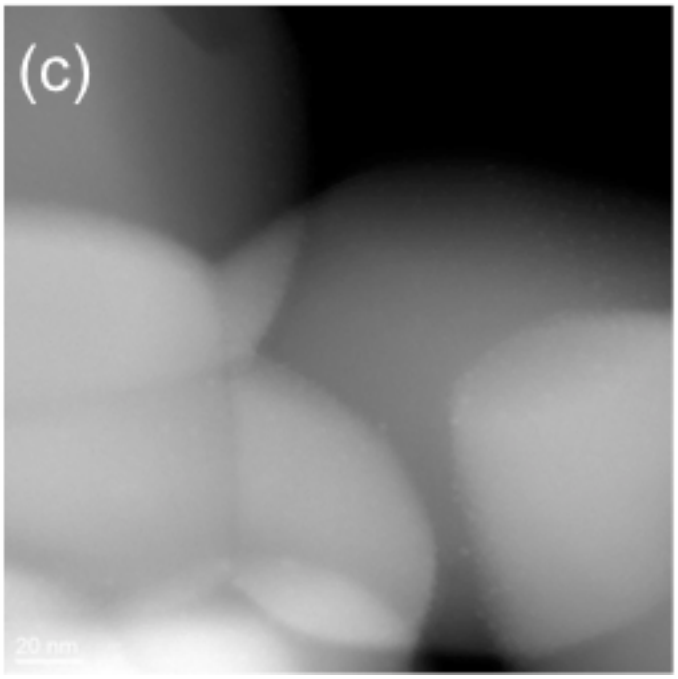

FIG. VII-5. STEM image attempts to make bigger Ag on anatase at various conditions (a) at 32 sec of reaction (b) higher light intensity (c) higher light intensity for 90 sec reaction time.

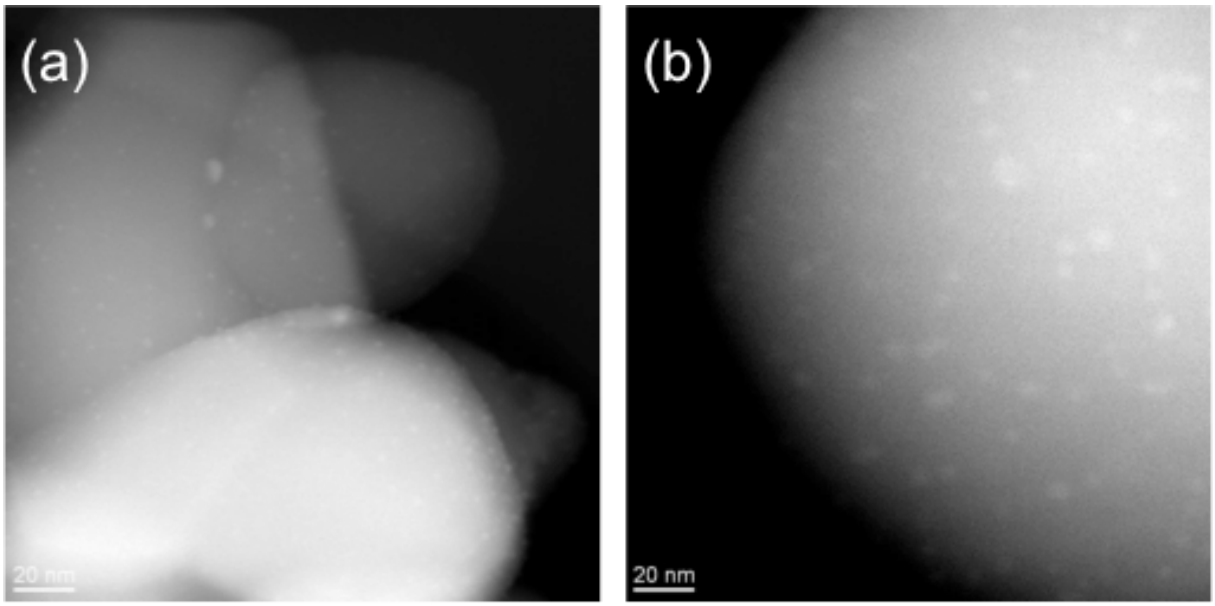

FIG. VII-6. STEM images of bigger Ag on anatase

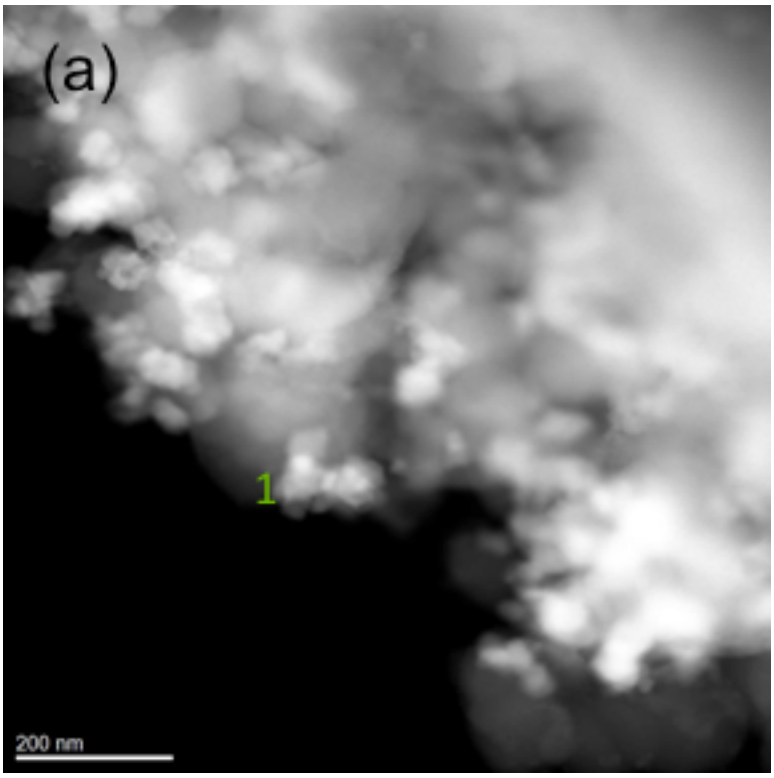

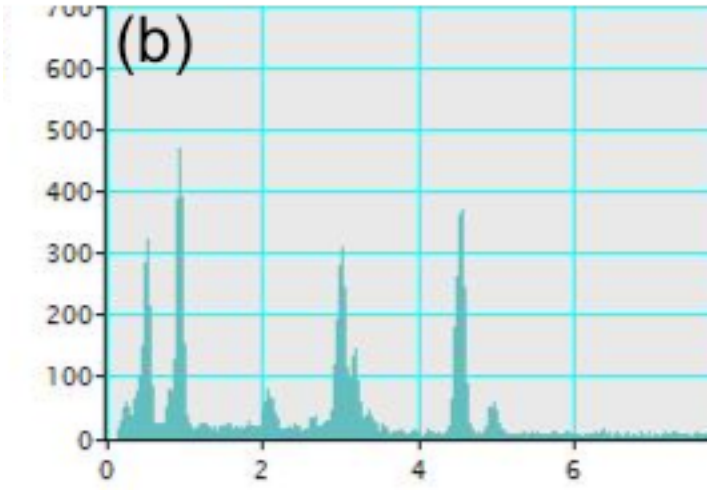

FIG. VII-7. STEM image of Pt photoreduction of 10 minutes onto Ag deposited anatase support. (b) EDS obtained from spot indicated presence of both Pt (2.0 eV) and Ag (2.9 eV)

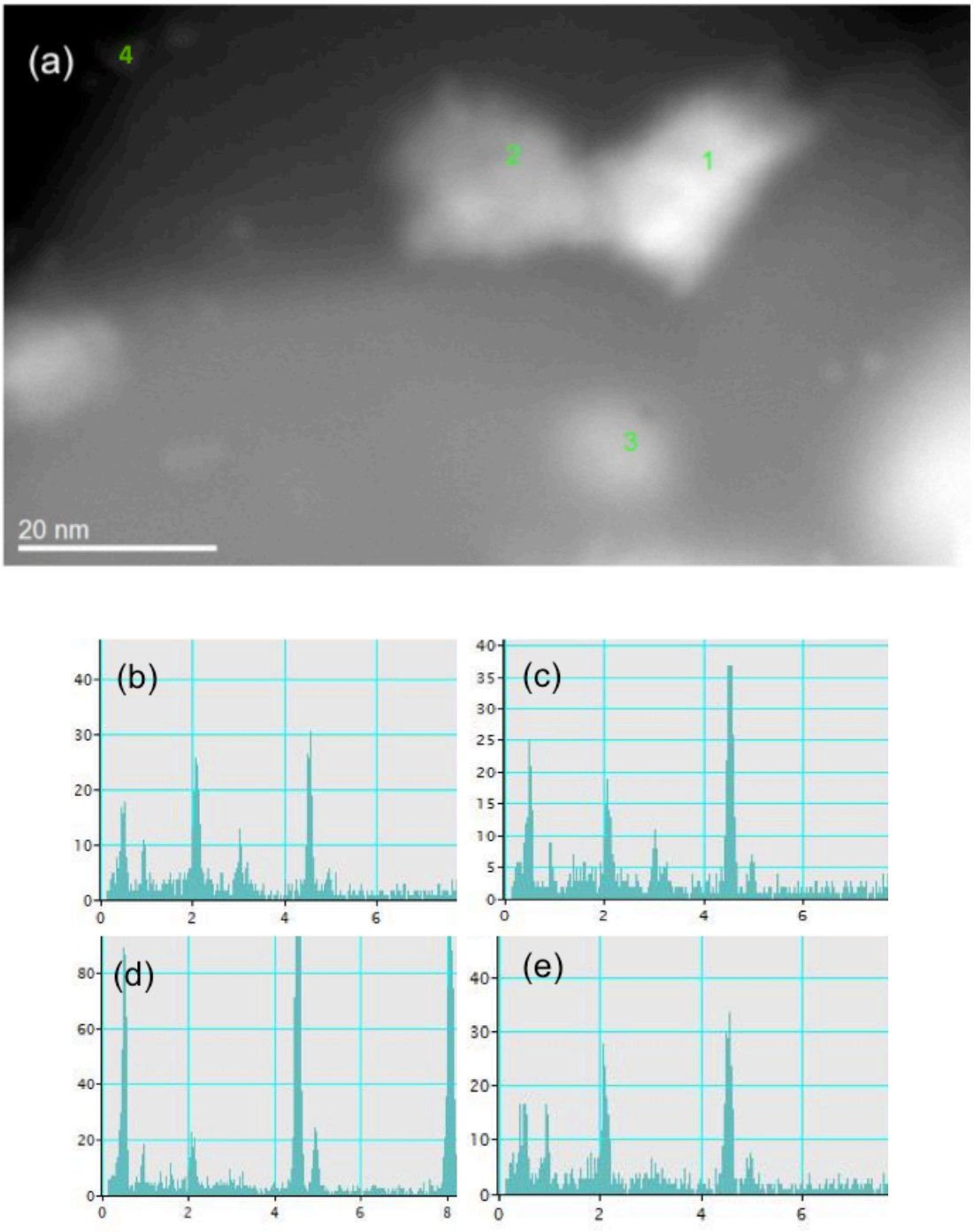

FIG. VII-8. Pt photoreduction after 35 minutes onto Ag deposited anatase support. (b) through (e) are the EDS obtained from spots 1 through 4 respectively.

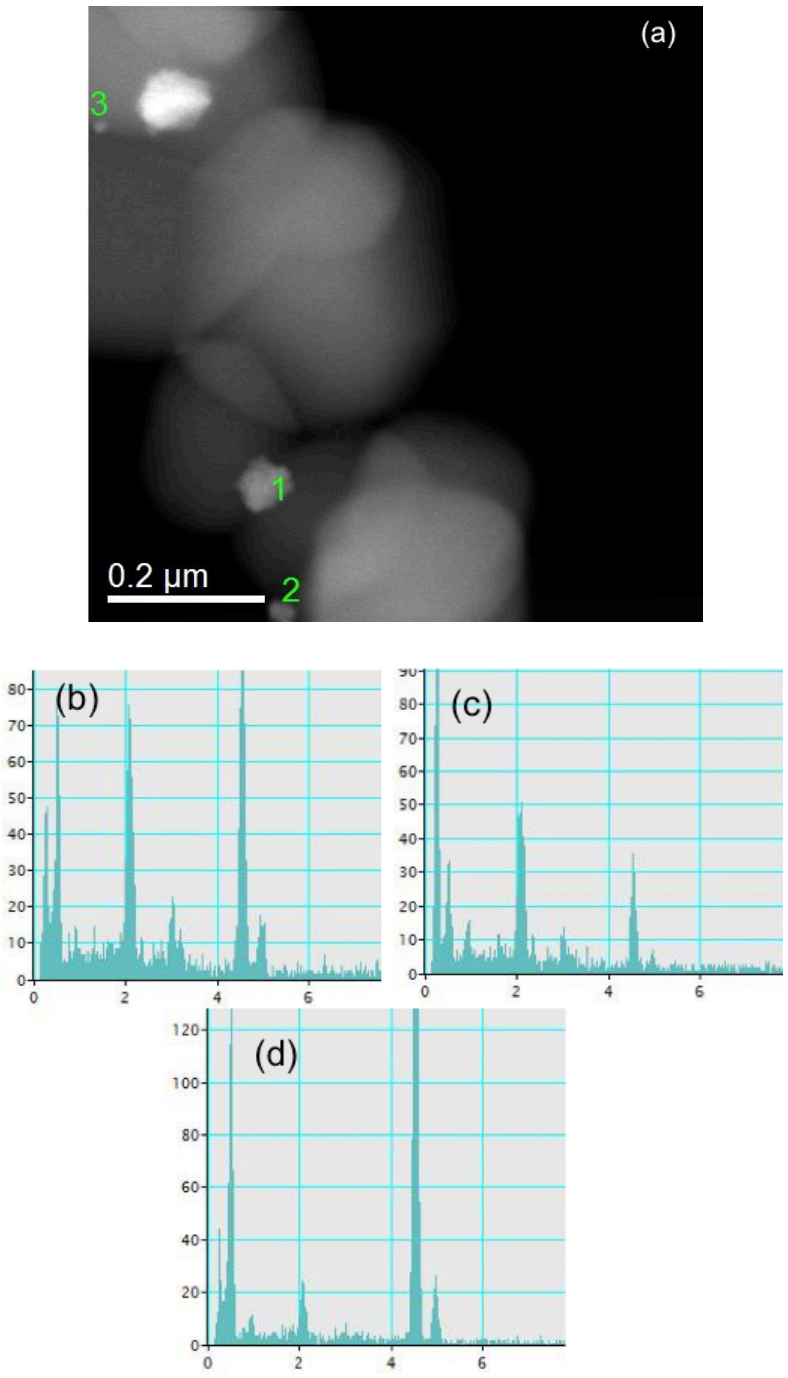

FIG. VII-9. Same reaction continued upto 45 minutes. (b) to (d) are the EDS obtained from spots 1 through 3 as in the image.

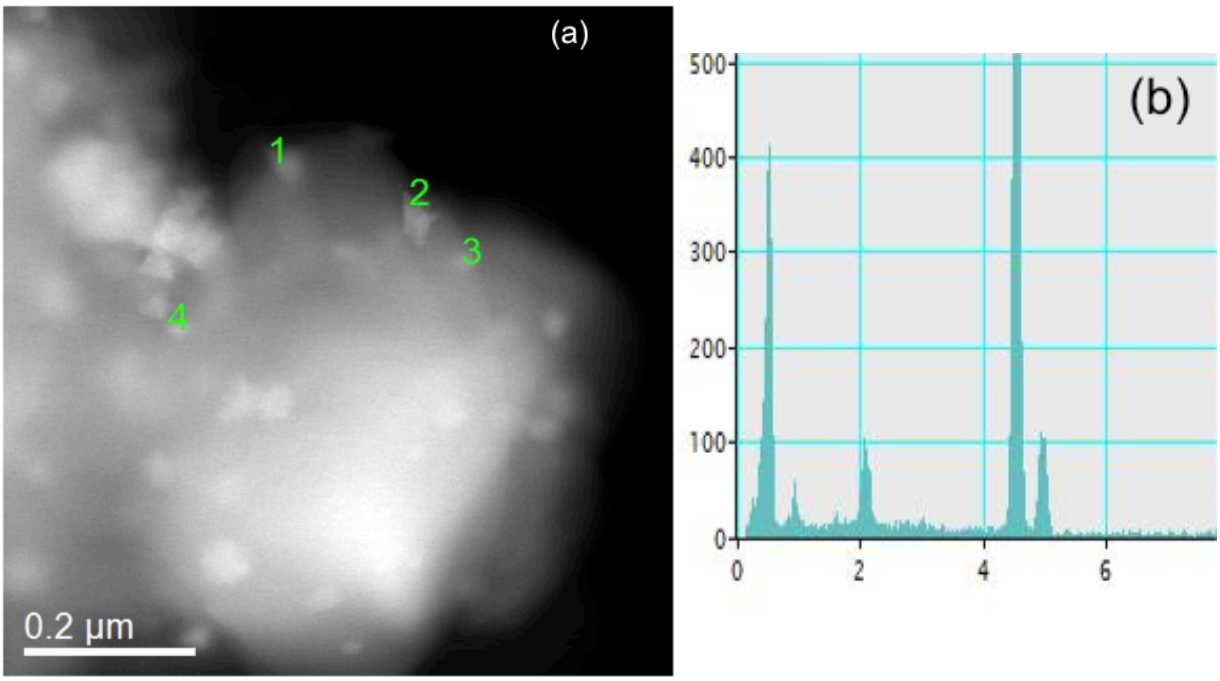

FIG. VII-10. Another set of clusters after reaction time 45 minutes, EDS (fig 10 b) collected from spot 4 in the sample shows an independent Pt particle formation.